POLITECNICO DI TORINO

MASTER OF SCIENCE IN GEO RESOURCES AND GEO ENERGY ENGINEERING

MASTER's DEGREE THESIS

HIGH SURFACE AREA NANO STRUCTURES FOR ELECTROCHEMICAL REDUCTION OF CARBON DIOXIDE

Candidate

Asjad Parvez
S348604

Supervisors

Prof. Candido Pirri

Prof. Juqin Zeng

Co-Supervisors

Prof. Candido Pirri

Prof. Mitra Bagheri

Academic Year: 2024/2025

Abstract

The electrochemical reduction of carbon dioxide into value-added fuels and chemicals presents a promising pathway toward carbon neutrality and renewable energy storage. Among emerging electrocatalysts, Cu-MOFs have attracted significant attention due to their tunable structures, high surface area, and ability to promote multi carbon product formation. In this study, Cu-MOF catalysts were synthesized via autoclave and microwave-assisted methods to investigate the influence of synthesis ramp time, hold time, and carbon source effect on catalytic performance and product selectivity. Microwave synthesis parameters were systematically varied to evaluate their impact on electrocatalytic CO_2 reduction.

To further understand carbon source effects, Cu-MOF was integrated with Vulcan carbon and mesoporous carbon under identical and different synthesis conditions. Product analysis using gas chromatography revealed distinct selectivity trends. Current density also played a decisive role in product distribution.

Overall, this work demonstrates that microwave ramp engineering and carbon source selection are effective strategies for tuning Cu-MOF electrocatalysts toward desired products. The insights gained provide a foundation for the rational design of MOF-derived catalytic systems aimed at efficient carbon utilization and sustainable electro fuel generation

Acknowledgements

This work stands as the final milestone of my university career. The research carried out over the past months at Italian Institute of Technology would not have been possible without the invaluable support of Prof. Mitra Bagheri whose contribution extended through every phase of this thesis from experimental laboratory activities to the final preparation of the manuscript. For this, I express my sincere gratitude.

I would like to extend special thanks to Prof. Dr. Juqin for granting me the opportunity to work at Italian Institute of Technology and to explore the fascinating field of electrochemical CO_2 reduction.

This milestone would have been impossible to achieve without the constant and unconditional support of my family, who stood by me despite the physical distance, even from far here in Turin.

CONTENTS

1- INTRODUCTION

1.1 Role of CO_2 as a Radiative Forcing Agent

The Sun sends energy to Earth, but not all of it is used. Some sunlight is reflected into space by clouds and the atmosphere, while the rest is absorbed by the Earth's surface. The Earth then gives off this energy as heat, which is trapped by greenhouse gases in the atmosphere. This natural "greenhouse effect" keeps our planet warm enough to support life. However, human activities release extra greenhouse gases, such as carbon dioxide, methane, nitrous oxide, water vapor, and fluorinated gases, which make the effect stronger and lead to global warming. Unlike nitrogen and oxygen, which cannot absorb much heat because of their simple two-atom structure, greenhouse gases contain three or more atoms that easily absorb and re-release heat, causing it to stay near the Earth's surface.

Among all greenhouse gases, carbon dioxide is the most critical driver of anthropogenic climate change. It accounts for more than two-thirds of total greenhouse gas emissions and contributes the largest share of positive radiative forcing on Earth's energy balance. The accumulation of CO_2 in the atmosphere is primarily the result of fossil fuel combustion, industrial processes such as cement production, and large-scale deforestation. This unprecedented growth has caused global average temperatures to increase by more than 1.1 °C above pre-industrial levels, triggering widespread environmental, economic, and social impacts. According to National Oceanic and Atmospheric Administration Earth System Research Laboratory [1] between 1990 and 2023, the Annual Greenhouse Gas Index rose by 51%, reflecting the growing warming influence of CO_2 and other gases. CO_2 alone accounted for roughly 42% of that increase underscoring its outsized effect on Earth's energy balance.

1.2 Carbon Capture Utilization and Storage

Mitigating the effects of CO_2 requires a combination of technological, natural, and policy-driven strategies. At the source, emissions can be reduced by transitioning from fossil fuels to renewable energy such as solar, wind, and hydropower, improving energy efficiency, and electrifying sectors like transport. Carbon capture, utilization, and storage technologies offer another approach, where CO_2 is captured from industrial processes and either stored underground or converted into useful products such as fuels, chemicals, or building materials. Nature-based solutions, including afforestation, reforestation, soil carbon sequestration, and the restoration of ecosystems like wetlands and mangroves, play a vital role in enhancing natural carbon sinks. Emerging technologies such as direct air capture and bioenergy with carbon capture and storage also hold promise for achieving negative emissions. Policy measures, including carbon pricing, subsidies for clean energy, and international agreements like the Paris Agreement, are essential to drive large-scale change, while lifestyle and behavioural adjustments such as sustainable consumption, reduced meat intake, and increased reliance on public transport can further contribute to lowering CO_2 emissions.

To lower atmospheric CO_2 to safe levels, it must be captured and transformed into other useful products. This approach not only reduces the carbon footprint of fossil fuel use but can also turn waste CO_2 into valuable chemicals. The CO_2 reduction reaction is one way to achieve this and can be carried out by chemical, photochemical, electrochemical, biological, or inorganic methods.

This study focuses on the electrochemical reduction of CO_2, because it has important advantages. It can use green electrolytes [3] and electricity from renewable sources, so the process itself does not add CO_2 emissions. Also, the conversion rate can be controlled simply by adjusting the applied electrode potential [4, 5], and the process can be scaled up for industrial applications. Electrochemical CO_2 reduction is a non-spontaneous reaction, meaning it only happens when external electrical energy is applied in an electrolytic cell. Such a cell has three main parts: an anode where oxidation occurs, a cathode where CO_2 reduction happens, and an electrolyte between them. By applying a voltage across

the electrodes, normally stable molecules like CO_2 can be reduced into other compounds.
The amount of energy needed for reduction or oxidation is measured using standard electrode potentials E^0, usually compared to the standard hydrogen electrode, which is defined as 0.00 V under standard conditions 25 °C, hydrogen gas at pressure 1 atm, and acidic solution at pH 0. However, since SHE conditions are hard to maintain and depend on pH, scientists often use the reversible hydrogen electrode instead. Potentials measured against different reference electrodes can be converted to reversible hydrogen electrode values using the Nernst equation:

$$E\ (V\ vs.RHE) = E_{(vs.\ ref:)} + E^0{}_{ref.(V)} + 0.059\ \ pH \qquad (1.1)$$

This allows electrode potentials to be compared across different electrolytes and pH conditions.

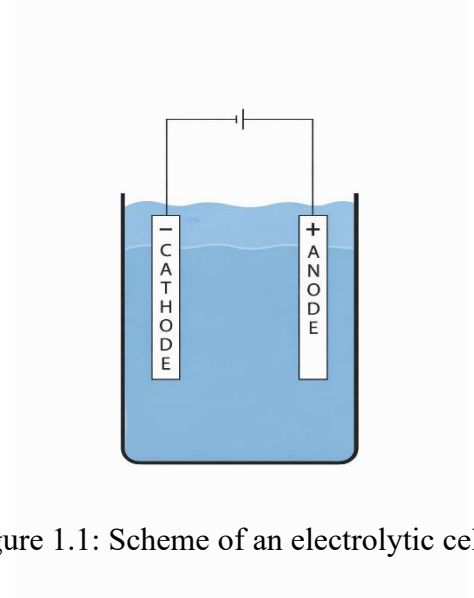

Figure 1.1: Scheme of an electrolytic cell

1.3 Research Objective

The aim of this work is to design and synthesize copper-based nanostructured catalysts through microwave-assisted synthesis and autoclave, using copper acetate and 2-methylimidazole as precursors, to investigate their performance in the electrochemical reduction of carbon dioxide. The motivation behind this study lies in the urgent need to mitigate rising atmospheric CO_2 levels by transforming this greenhouse gas into valuable chemicals and fuels. Special focus is placed on copper, as it is the only metal capable of producing multi-carbon products such as ethylene and ethanol, although its low selectivity remains a major challenge. By tailoring synthesis parameters, including temperature, ramp time, solvent composition, and drying conditions, this work seeks to optimize catalyst morphology, surface properties, and stability. The final goal is to develop efficient, scalable, and sustainable copper-based materials that can improve the selectivity and efficiency of CO_2 reduction toward high-energy-density products, contributing to carbon recycling and the transition to clean energy systems.

2- ELECTROCHEMICAL TRANSFORMATION OF CO_2

2.1 CO_2 reduction reaction pathways

CO_2 is a very stable molecule, with a binding energy of 750 kJ/mol, much higher than that of C–H (411 kJ/mol), C–C (336 kJ/mol), or C–O (327 kJ/mol) bonds. This strong C=O double bond makes its activation the most energy-demanding step in any reduction process [6, 7]. To overcome this barrier, catalyst design and material engineering are employed to lower the required energy and promote the reaction. As summarized in Table 2.1, electrochemical CO_2 reduction reactions in aqueous media proceeds through a series of electron and proton transfer steps [5, 6], which can generate a wide range of products. These products are generally classified into two groups: C1 species containing a single carbon atom and C2 species containing two carbon atoms. The C1 group consists of carbon monoxide, formic acid, formaldehyde, methanol, and methane. The C2 group includes oxalic acid, ethylene, ethane, and ethanol. Under specific conditions, even larger hydrocarbons with more than two carbons may also be formed.

Table 2.1: Standard reduction potentials of selected products [6]

.

Compound	Reaction Pathway	E^0 [V vs. SHE]
CO	$CO_2 + 2e^- + 2H^+ \rightarrow CO + H_2O$	E^0 = - 0.106 V
HCOOH	$CO_2 + 2e^- + 2H^+ \rightarrow HCOOH$	E^0 = - 0.250 V
CH_3OH	$CO_2 + 6e^- + 6H^+ \rightarrow CH_3OH + H_2O$	E^0 = + 0.016 V
CH_4	$CO_2 + 8e^- + 8H^+ \rightarrow CH_4 + 2H_2O$	E^0 = + 0.169 V
C_2H_4	$2CO_2 + 12e^- + 12H^+ \rightarrow C_2H_4 + 4H_2O$	E^0 = + 0.064 V
$CO_2O_4^{2-}$	$2CO_2 + 2e^- \rightarrow CO_2O_4^{2-}$	E^0 = - 0.590 V
H_2	$2H^+ + 2e^- \rightarrow H_2$	E^0 = 0.00 V

According to Xie et al. [6], the mechanism on a catalyst surface generally involves three key stages:

1. Adsorption and interaction of CO_2 molecules with the active sites on the catalyst surface.
2. Activation and reduction of the adsorbed CO_2, initiated by the catalyst.
3. Desorption of the products and regeneration of the catalyst's active sites.

2.2 Catalyst Role

The first electron transfer to adsorbed CO_2, forming the radical $CO_2^{\bullet-}$, is considered the rate-determining step on transition metal catalysts because it requires a high activation energy [6]. Due to this barrier, CO_2 cannot be directly reduced to other products at the theoretical potentials, and an additional energy input called the overpotential is required [8]. This extra energy comes not only from CO_2 activation but also from ohmic losses in the electrolyte/electrodes and mass transport limitations.

The catalyst plays two main roles: (i) lowering the overpotential so that the reaction can proceed with less supplied energy, and (ii) improving selectivity toward CO_2 reduction over the competing hydrogen evolution reaction, which occurs at similar potentials [4,8]. Once $CO_2^{\bullet-}$ is formed, its interaction with the catalyst surface dictates which products are obtained. For example, on Au, Ag, Zn, and Ga, $CO_2^{\bullet-}$ binds via the carbon atom, forming *COOH intermediates that lead to CO, which desorbs easily due to weak binding. On Sn, In, Pb, Hg, and Cd, $CO_2^{\bullet-}$ binds through oxygen, favoring $HCOO^-$ and then formic acid. Cu behaves differently, as its moderate *CO binding allows the formation of CO, format, and even hydrocarbons. In contrast, metals like Ni, Fe, Pt, and Ti mainly drive hydrogen production instead of CO_2 reduction reaction [8]. Although several pathways exist, CO_2 reduction to CO is often the most kinetically favourable, as it only requires two electrons [8]. This explains why much research has focused on finding cheaper alternatives to Au and Ag electrodes for practical and scalable applications.

2.3 CO_2 reduction reaction efficiency parameters

When evaluating an electrocatalyst, the current density (j) is the most common parameter used to describe the reaction rate at the electrode. It represents the electric current per unit surface area of the electrode. In general, a higher current density at a given potential indicates a faster reaction rate. For this an effective catalyst should deliver high current density toward the desired product while operating at relatively low overpotential. Besides activity and overpotential, selectivity is also crucial. As discussed earlier (Section 2.1), CO_2 can be reduced into different products, while hydrogen often appears as a side product. The selectivity of a catalyst is usually expressed as the faradaic efficiency which is defined as the fraction of the total charge that contributes to forming a specific product over the total charge passed during the reaction.

$$\text{FE}(\%) = \frac{nNF}{Q} 100$$

Here, n represents the number of electrons participating in the faradaic reaction, N is the quantity of product formed, F is the Faraday constant (96485.33 C/mol), and Q is the total charge passed during the process. For instance, in the case of CO production like hydrogen evolution reaction, two electrons are involved in the reaction.

$$\text{FE(CO)} = \frac{2 \times F \times mol\ CO\ produced}{j \times A \times t}$$

The efficiency and product distribution depend on several factors. As discussed on Sec. 2.2, the choice of catalyst, especially its electronic surface properties, strongly influences both efficiency and selectivity. In addition, the particle size of the catalyst affects its reactivity and selectivity by changing the type and number of active sites (see Sec. 2.5.1 for details). This size-related effect has been studied, both theoretically and experimentally, for metals such as Cu, Ag, and Au.

Certain catalyst structures, such as dendrite-like forms, can improve mass transfer of CO_2 to the surface, making the reaction more efficient [5]. The design of the electrolytic cell also plays an important role, as it influences charge transfer and therefore the efficiency of reaction. Since no standard configuration exists, it is often difficult to directly compare results from different experiment setups [8]. The main objective remains to perform CO_2 reduction efficiently while keeping the overpotential as low as possible.
The electrolyte, usually an aqueous solution containing cations (Na^+, K^+) and anions (HCO_3^- or OH^-), strongly affects both current density and product selectivity. Higher conductivity improves current density, while the pH near the electrode influences overpotential and product distribution [8].

Reaction conditions such as pressure and temperature also impact. Increasing temperature generally

lowers overpotential because of higher conductivity and better contact between electrode and electrolyte, but at the same time reduces CO_2 solubility, limiting the available reactant [8]. Higher pressure increases CO_2 solubility but requires more complex cell designs that can operate safely under such conditions [8].

Overall, an effective material for CO_2 reduction should meet the following requirements:

- High current density (fast reaction rate)
- Low overpotential (good energy efficiency)
- High faradaic efficiency for the target product (selectivity)
- Strong stability and long durability
- Low cost of both raw materials and electrode fabrication

2.4 CO_2 reduction reaction challenges

CO_2 reduction is difficult because CO_2 is thermodynamically very stable, with strong C=O bonds that require high overpotentials for activation. The reaction mechanism is complex, involving multiple electrons and proton transfers that can form various intermediates and products, making selectivity a major challenge. Faradaic efficiency is an important measure of how effectively the applied current drives the desired reaction, but efficiency often drops due to competing side reactions such as the hydrogen evolution reaction which is easier and occurs at similar potentials. In addition, catalyst stability is limited by electrode poisoning from intermediates or electrolyte impurities that block active sites. Metal based catalysts each show specific limitations Au, Ag, and Zn mainly produce CO while Sn, In, and Bi favor format; Pt, Ni, and Fe mostly produce hydrogen; while Cu is unique for producing hydrocarbons and oxygenates like methane and ethylene but still suffers from poor efficiency and long-term stability.

2.5 Cu-based catalysts

Copper and copper-based electrodes are unique because they are the only materials able to produce significant amounts of C2 products, such as ethanol and ethylene. However, their main limitation is low selectivity, as a wide variety of products are typically formed. For this reason, research on copper focuses on optimizing its properties to improve productivity toward high-energy-density products. Several factors strongly influence catalytic behaviour. For example, when copper nanoparticles are smaller than 5 nm, they tend to favour the formation of H_2 and CO, while the production of hydrocarbons decreases. In contrast, shorter inter-particle distances increase the selectivity toward hydrocarbons. The crystalline orientation of the surface is also important the Cu (100) facet promotes the formation of ethylene, whereas the Cu (111) facet Favors methane. A higher surface area, achievable through porous structures, enhances the generation of C2+ compounds, while the introduction of defects through methods such as doping, etching, or partial oxidation can suppress the competing hydrogen evolution reaction and steer selectivity toward desired products. Copper acetate Cu $(CH_3COO)_2$ is commonly employed as a precursor in the preparation of these catalysts, as it can be easily converted into copper nanoparticles or oxides. By controlling how copper acetate is processed for instance, through microwave synthesis, calcination, or doping the size, porosity, and surface properties of the resulting copper catalyst can be tuned, enabling improved performance in CO_2 reduction toward multi-carbon products. After it was discovered that plasma oxidized Cu foils could be used for some control over product distribution, research focused on developing more active Cu-based catalysts [6]. Advances in nanoparticle synthesis controlling size, shape, structure, and composition have shown that nanostructured Cu electrodes provide higher selectivity and activity. Factors such as size, porosity, alloying, and support materials all play a key role in their performance.

2.5 .1 Morphology effect

The performance of plasma-oxidized Cu foils has been linked to metastable grain boundaries on their surface. This observation led researchers to study porous Cu structures to better control pathways. For example, Cu nano-foams made by electrodeposition with H_2 bubbles as a template showed improved production of HCOOH and CO compared to smooth Cu electrodes [9].To investigate the effect of pore size, ordered nano-porous Cu structures were created using Al_2O_3 templates. Results showed that smaller and deeper pores favoured the formation of C2 products like C_2H_4 and C_2H_6, while wider pores produced mainly CO and CH_4 [10]. The explanation is that narrow pores slow down ion diffusion, increase local pH, and encourage C–C coupling, but at the same time can limit mass transport to the catalyst's active sites.
Nanoparticles have also been explored to overcome these limitations. Their catalytic properties depend strongly on size and surface structure because atoms at corners, edges, and different crystal planes behave differently [6]. Studies on Cu found that larger particles (6-18 nm) were more selective for hydrocarbons like CH_4, while very small (<6 nm) favored H_2 and CO production. This difference is due to surface atom coordination: larger particles have more stable, highly coordinated atoms that promote hydrocarbon formation, while smaller ones expose more low-coordinated atoms that bind CO and H too strongly, preventing further hydrogenation [6].

2.5 .2 Cu-based MOFs

It is a well-established class of crystalline porous materials formed by coordination of Cu^{2+} ions with organic linkers such as carboxylates or imidazolates. The benchmark example is HKUST-1 ($Cu_3(BTC)_2$) [2] which features Cu paddlewheel clusters and benzene-1,3,5-tricarboxylate ligands. Cu-MOFs are of interest due to their high surface area, tuneable pore structures, and redox-active Cu sites, making them valuable for adsorption, gas separation, and catalytic applications. Overall, Cu-MOFs are not only functional materials in their pristine crystalline form but also powerful precursors for deriving Cu/carbon nanocomposites. Their flexibility in structure and post-synthetic modification makes them highly attractive for applications in energy storage, electrocatalysis, and environmental remediation. Zeolitic imidazolate frameworks are a subclass of MOFs in which metal ions are bridged by imidazolate ligands, producing zeolite-like topologies with high stability and porosity [11]. Among them, Cu-ZIFs, prepared by coordinating Cu^{2+} ions with imidazolate derivatives such as 2-methylimidazole, have attracted attention because they combine the tuneable pore structure of ZIFs with the redox activity of copper (Cu^{2+}/Cu^{+}). This dual functionality makes Cu-ZIFs valuable in catalysis, energy storage, and sensing.

2.5 .3 Crystal facets and selectivity

Several studies using single-crystal copper electrodes have shown that the way different crystal faces (facets) are exposed can strongly influence which products are formed during CO_2 reduction [6,12]. This is because atoms on each facet have slightly different properties. For instance, the Cu (111) surface tends to produce mostly methane and sometimes CO, while facets like Cu (100), (110), (911), and (711) are more favourable for generating C2 products such as ethylene and ethanol. This means that by carefully controlling the shape of copper nanoparticles, researchers can tune which reaction products are favoured. As discussed in Section 2.4, particle shape also affects the overall reaction rate, since certain structures can make it easier for CO_2 molecules to reach and react on the active sites [5].

2.5 .4 Cu-MOF on carbon-based materials

To overcome intrinsic conductivity and limited structural stability researchers have developed Cu-MOF/carbon composites, where Cu-MOFs are integrated with conductive carbon-based materials such as graphene oxide, reduced graphene oxide, carbon nanotubes, activated carbon, and hierarchical

porous carbons [13]. The incorporation of carbon not only enhances electrical conductivity but also improves the mechanical and chemical stability of the composite while maintaining the high surface area and porosity of the MOF. Moreover, carbon matrices provide additional pathways for electron transport, prevent MOF particle agglomeration, and facilitate uniform dispersion of copper active sites. Such Cu-MOF/carbon composites have demonstrated excellent performance in CO_2 reduction, oxygen reduction reactions, hydrogen evolution, supercapacitors, batteries, and pollutant adsorption**.** Structural studies often reveal that the crystalline peaks of Cu-MOF are partially preserved in these composites but are broadened or reduced in intensity due to strong MOF/carbon interactions. In some cases, a broad hump around 20-25° in XRD patterns confirms the presence of amorphous carbon. Upon thermal treatment or carbonization, Cu-MOFs can further transform into Cu, Cu_2O, or CuO nanoparticles embedded in a conductive carbon matrix, resulting in highly active and durable functional materials. Overall, Cu-MOF/carbon composites represent a synergistic platform that combines the advantages of porosity, tunable structure and redox sites with those of carbon conductivity, stability, and mechanical support, making them highly relevant for next-generation energy and environmental technologies [14].

2.5. 5 Role of secondary metals in Cu catalysts

Research has shown that combining copper with other metals can change the selectivity by altering the chemical environment around Cu atoms and adjusting the binding of key intermediates such as $^*CO$, $^*COOH$, and $^*CHO$ [15]. The outcome strongly depends on the type of second metal and the new active sites formed on the surface. When Cu is alloyed with Au, Ag, Zn, or Cd, the reaction mainly produces CO, often with higher faradaic efficiency than pure Cu. This is linked to Cu's ability to stabilize $^*COOH$, the weak binding of $^*CO$ on these metals, and their low affinity for hydrogen, which helps suppress hydrogen evolution reaction. Pairing Cu with Sn or In can give either CO or formic acid, depending on which metal dominates the active sites. If Sn or In are more active, HCOOH is favored through $^*OCHO$ stabilization if Cu is more active, CO becomes the main product.

In Cu/Pd systems, the structure is very important. Ordered alloys such as Pd_7Cu_3 or $CuPd_3$ mainly produce CO with efficiencies up to 90%, while phase-separated Cu/Pd nanoparticles favour C2 products due to C–C coupling on Cu sites. Cu combined with Pt or Ni has also been reported to generate CH_4 and C_2H_4, though with relatively low efficiencies, and only a few studies exist [15]. Overall, the selectivity and efficiency of Cu-based alloys are determined by how the additional metal changes the binding energies of the intermediates on the catalyst surface [15].

2.5. 6 Support material effect

Copper nanoparticles usually need to be placed on a support to prevent them from clumping together and to maintain good electrical conductivity. Common supports include carbon black, carbon nanotubes, and graphene, though other materials like MoS_2 and polyaniline are also being explored [6]. For instance, 7 nm Cu nanoparticles tested on regular carbon supports mainly produced ethylene with faradaic efficiency with 6.3% at -1.1 V. However, when the same particles were supported on nitrogen-doped graphene, the reaction products varied with the applied potential at -0.8 V, formic acid with faradaic efficiency 62% was favored, while at -0.9 V, more hydrocarbons such as CH_4, C_2H_4, and C_2H_6 were formed, with a higher selectivity toward C_2H_4 up to 19% faradaic efficiency. This difference is attributed to the pyridinic nitrogen sites in the graphene, which act as Lewis bases, attracting more protons around the Cu atoms and facilitating C–C coupling as well as the conversion of COOH into CO and then CHO^* [6].

3- MATERIALS AND METHODS

This chapter provides a detailed overview of the materials and experimental procedures employed for the synthesis and characterization of the samples studied. The complete compositional details of each synthesized material are reported (Table 3.1) where the proportion of the precursors are clearly specified. These compositional variations were intentionally designed to investigate their influence on the morphological, structural, and electrochemical properties of the final products.

The chapter also describes the preparation of the precursor solutions, mixing procedures, and post-synthesis treatments used to obtain homogeneous and stable nanostructured materials. The methodology ensures accurate control over the morphology and composition of the products, providing the foundation for the subsequent structural and electrochemical evaluations. In addition, the experimental setup for material characterization is outlined. Techniques such as X-ray Diffraction for crystallographic analysis and Field emission electron microscopy for morphological analysis. The procedures for the fabrication of working electrodes and the corresponding electrochemical measurements including Electrochemical Impedance Spectroscopy, Linear Sweep Voltammetry, and Chronopotentiometry are also described, emphasizing the applied potential ranges, electrolyte composition, and electrode configurations.

3.1 Catalyst precursor solutions preparation

For sample AP1 Cu-MOF (RAMP 20′ HT 30′) and AP5 Cu-MOF (RAMP 5′ HT 30′) solution was prepared by dissolving 0.454 g copper acetate in 10 mL of deionized water and 10 mL of ethanol. The mixture was prepared using a magnetic stirrer for approximately 5 minutes until the solid particles completely dissolved forming a light blue solution. Subsequently 2g 2-methylimidazole (Table 3.1) was added to the solution followed by the addition of the remaining 10 mL of deionized water and 10 mL of ethanol. The mixture was stirred continuously until it was fully dissolved resulting in a final dark blue solution (Figure 3.1).

In the case of sample AP3 Cu-MOF/Vulcan carbon (RAMP 20′ HT 30′), AP4 Cu-MOF/Vulcan carbon (RAMP 5′ HT 30′), AP6 Cu-MOF/Vulcan carbon, and AP7 Cu-MOF/Vulcan carbon, first 0.18 g of Vulcan carbon (Table 3.1) solution was prepared in 5 mL deionized water and 15 mL ethanol. In parallel 0.454 g of copper acetate was dissolved in 15 mL of deionized water and 5 mL of ethanol. The mixture was stirred magnetically for about 5 minutes until the solid fully dissolved forming a light blue solution. Then, 2 g of 2-methylimidazole was added and stirred until completely dissolved. Then mix well both solutions together and final sample solution prepared for synthesis (Figure 3.1).

Figure 3.1: Magnetic stirrer and Branson ultra sonic cleaner for precursor solutions preparation

For sample AP8 Cu-MOF/Vulcan carbon, firstly carbon dispersion was done by dissolving 0.18 g of Vulcan carbon (Table 3.1) in 5 mL of deionized water and 15 mL of ethanol, followed by ultrasonication in a Branson ultrasonic cleaner for 30 minutes to ensure uniform dispersion. In parallel 0.454 g of copper acetate was dissolved in 15 mL of deionized water and 5 mL of ethanol. The mixture was stirred magnetically for about 5 minutes until the solid fully dissolved forming a light blue solution. Then, 2 g of 2-methylimidazole was added and stirred until completely dissolved. The resulting mixture was sonicated in with first solution for an additional 15 minutes to achieve complete homogenized final solution (Figure 3.1).

In case of sample AP9 Cu-MOF/Mesoporous carbon (RAMP 5′ HT 30′) first solution was prepared by dissolving 0.09 g of mesoporous carbon in 5 mL deionized water and 5 mL ethanol. In parallel 0.227 g of copper acetate (Table 3.1) was dissolved in 5 mL of deionized water and 5 mL of ethanol. It was stirred magnetically for about 5 minutes until the solid fully dissolved forming a light blue solution. Then, 2 g of 2-methylimidazole was added and stirred until completely dissolved. Then both solutions well mixed together and final sample solution prepared for synthesis (Figure 3.1).

Table 3.1: Composition details of catalyst precursor solutions.

Sample	Copper (II) acetate	2-Methylimidazole	DI Water: Ethanol (ml)	Carbon Source
AP1 Cu -MOF (RAMP 20′ HT 30′)	0.454 g	2 g	20:20	0
AP3 Cu -MOF/ Vulcan carbon (RAMP 20′ HT 30′)	0.454 g	2 g	20:20	0.18 g Vulcan carbon
AP4 Cu -MOF/ Vulcan carbon (RAMP 5′ HT 30′)	0.454 g	2 g	20:20	0.18 g Vulcan carbon
AP5 Cu -MOF (RAMP 5′ HT 30′)	0.454 g	2 g	20:20	0
AP6 Cu -MOF/ Vulcan carbon (RAMP 20′ HT 5′)	0.454 g	2 g	20:20	0.18 g Vulcan carbon
AP7 Cu-MOF/ Vulcan carbon	0.454 g	2 g	20:20	0.18 g Vulcan carbon
AP8 Cu -MOF/ Vulcan carbon	0.454 g	2 g	20:20	0.18 g Vulcan carbon
AP9 Cu -MOF/ Mesoporous carbon (RAMP 5′ HT 30′)	0.227 g	1 g	10:10	0.09 g Mesoporous carbon

Following the preparation procedures, all samples were obtained in solution form and made ready for the subsequent synthesis stage (Fig.3.2).

3.2 Microwave assisted synthesis

Metal organic frameworks represent an extensive and highly diverse class of materials. Their significant commercial potential stems from their exceptionally high porosity and tuneable pore environments, which provide outstanding capacity and selectivity for gas storage, separation, and hydrocarbon related applications. Proposed use spans several critical fields, including energy, environmental sustainability, and advanced healthcare. Despite their promise, large-scale adoption of MOFs in industry remains limited due to challenges in scaling up production and the relatively high economic and environmental costs compared to conventional sorbents. Therefore, developing efficient and sustainable manufacturing technologies is essential for enabling the transition of research from the laboratory to industrial implementation.

Microwave-assisted synthesis has emerged as a highly promising approach for scaling up MOFs production. This technique offers distinct advantages over conventional methods, including drastically reduced reaction times from hours to minutes, high space time yields, and improved energy efficiency. The most notable benefit of microwave heating lies in its precise control over properties such as morphology, particle size, and phase by adjusting the applied power and treatment duration [16].

The catalyst synthesis work was carried out using a Milestone flexi WAVE advanced flexible microwave synthesis platform (Fig.3.2). This system provides controlled microwave irradiation, allowing rapid and uniform heating of the reaction mixture. Compared to conventional heating methods, it offers significant advantages such as shorter reaction times, higher yields, and improved selectivity. In addition, the use of microwave heating contributes to greener chemistry by reducing solvent consumption, energy usage, and waste generation. The instrument is equipped with sensors to monitor temperature and pressure, ensuring safe and reproducible operation. These features make it particularly suitable for catalyst preparation, as the controlled heating environment promotes uniform nucleation and growth, leading to catalysts with enhanced crystallinity, smaller particle size, and higher surface area.

Figure 3.2: Milestone flexi WAVE advanced flexible microwave

The instrument settings included a maximum microwave power of 250 W and a maximum pressure limit of 250 psi that is equal to approximately 17.2 bar which were set as safety thresholds rather than as applied operating conditions (Tab.3.2). These limits ensured that the reaction proceeded under controlled and safe conditions. Since the same parameters were used for all five runs at 120 °C, 250W,

and 250 psi any variations in the obtained products can be attributed to the composition particularly carbon source and differences in the synthesis conditions (RAMP, Hold Time).

Table 3.2: Microwave operating parameters during synthesis.

Sample	RAMP (minutes)	Hold Time(minutes)	Temperatue °C	Power W	Pressue bar
AP1 Cu -MOF (RAMP 20′ HT 30′)	20′	30′	120	250	17.2
AP3 Cu-MOF/Vulcan carbon (RAMP 20′ HT 30′)	20′	30′	120	250	17.2
AP4 Cu-MOF/Vulcan carbon (RAMP 5′ HT 30′)	5′	30′	120	250	17.2
AP5 Cu-MOF (RAMP 5′ HT 30′)	5′	30′	120	250	17.2
AP6 Cu -MOF/Vulcan carbon (RAMP 20′ HT 5′)	20′	5′	120	250	17.2
AP9 Cu-MOF/ Mesoporous carbon (RAMP 5′ HT 30′)	5′	30′	120	250	17.2

3.2.1 Sample AP1 Cu-MOF (RAMP 20′ HT 30′)

The sample was placed in the microwave reactor and subjected to the programmed synthesis conditions. A small magnetic stir bar was introduced into the solution to ensure uniform mixing and heat distribution during the reaction process. The temperature gradually increased to 120 °C within 20 minutes and maintained for a hold time of 30 minutes. Throughout the process, the maximum limits of 250 W power and 250 psi (≈17.2 bar) pressure were set, but the actual operating values remained significantly lower (Fig.3.2.1). The recorded data show that the pressure stabilized at around 3.4 bar, while the applied microwave power fluctuated between 56-73 W to sustain the reaction temperature (Table.3.2.1).

Figure 3.2.1: Microwave reactor control panel during synthesis of AP1 Cu-MOF **(**RAMP 20′ HT 30′)

After the completion of the hold period, the reactor cooled naturally and the final product solution of was obtained under these controlled conditions. Rember that when pressure drops up to 1 bar, we can open the microwave. After microwave-assisted synthesis the final product solution was collected from the reactor.

Table 3.2.1: Microwave control panel during synthesis of AP1 Cu-MOF **(**RAMP 20′ HT 30′)

Time	**Pressure** **bar**	**Temperature** **°C**	**Power** **W**
10:42 s	1.0	76	73
21:37 s	3.6	120	63
30:49 s	3.4	120	56
40:53 s	3.4	120	63
50:54 s	2.9	116	0
1:00	1.4	90	0

3.2.2 Sample AP3 Cu-MOF/Vulcan Carbon **(**RAMP 20′ HT 30′)

The sample was placed in the microwave reactor and subjected to the same programmed conditions as AP1 Cu-MOF **(**RAMP 20′ HT 30′). A bigger magnetic stir bar was used for uniform mixing. The temperature gradually increased to 120 °C within 20 minutes and maintained for a hold time of 30 minutes (Fig.3.2.2). Same as AP1 the maximum limits were set to 250 W power and 250 psi (≈17.2 bar) pressure, although the actual operating conditions were lower.

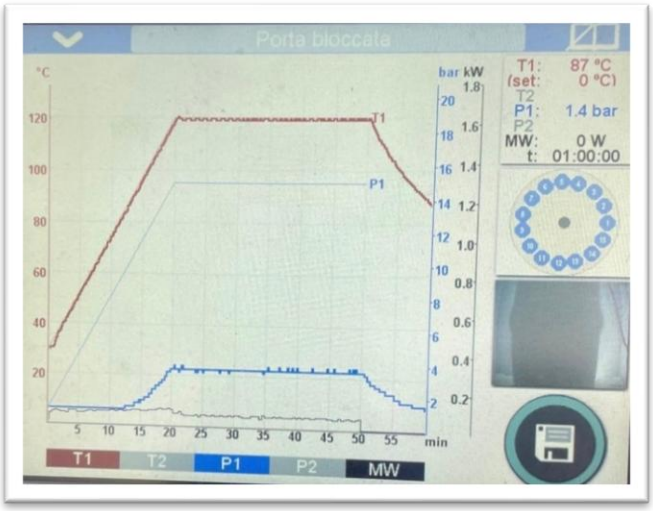

Figure 3.2.2: Microwave reactor control panel during synthesis of AP3 Cu-MOF/Vulcan Carbon **(**RAMP 20′ HT 30′)

The recorded data (Table 3.2.2) indicates that the pressure stabilized 3.6-3.8 bar during hold time, while the applied microwave power varied in the range of 26-69 W during the heating and holding stages to sustain the target temperature. After the reaction was completed and the system cooled down, the final product solution of AP3 Cu-MOF/Vulcan Carbon **(**RAMP 20′ HT 30′) was obtained under these controlled synthesis parameters.

Table 3.2.2: Microwave control panel during synthesis of AP3 Cu-MOF/Vulcan Carbon **(**RAMP 20′ HT 30′)

Time	**Pressure** **bar**	**Temperature** **°C**	**Power** **W**
10:08 s	1.0	76	69
20:09 s	3.8	121	26
30:34 s	3.6	120	52
40:03 s	3.6	120	48
50:53 s	3.1	116	0
1:00	1.4	87	0

After microwave-assisted synthesis the final product solution was collected from the reactor.

3.2.3 Sample AP4 Cu-MOF/Vulcan Carbon **(**RAMP 5′ HT 30′)

The prepared Sample was introduced into the microwave reactor and processed under the same programmed conditions as AP3 Cu-MOF/Vulcan carbon **(**RAMP 20′ HT 30′) only with lower RAMP that was 5 minutes (Fig.3.2.3). A magnetic stir bar was placed into the solution to ensure uniform mixing. The temperature gradually rose to 120 °C within 5 minutes and maintained for a hold time of 30 minutes. The maximum operational limits were again set at 250 W power and 250 psi (≈17.2 bar) pressure.

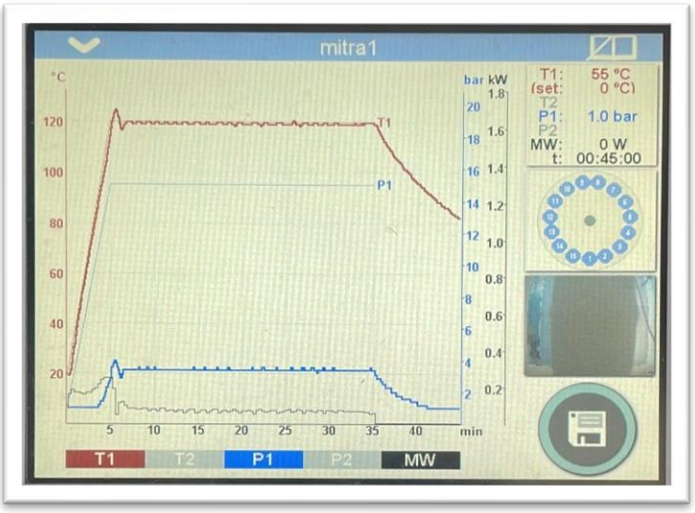

Figure 3.2.3: Microwave reactor control panel during synthesis of AP4 Cu-MOF/Vulcan Carbon **(**RAMP 5′ HT 30′)

The system data show that the pressure stabilized around 3.4 bar (Table.3.2.3). After the completion of the hold period, the reactor was cooled and the final product solution of AP4 Cu-MOF/Vulcan **(**RAMP 20′ HT 30′) Carbon obtained under these controlled conditions.

Table 3.2.3: Microwave control panel during synthesis of AP4 Cu-MOF/Vulcan Carbon **(**RAMP 20′ HT 30′)

Time	**Pressure** **bar**	**Temperature** **°C**	**Power** **W**
5:03 s	3.6	120	234
15:27 s	3.4	120	74
25:25 s	3.6	120	76
35:56 s	2.5	114	0
45:00 s	1.0	55	0

3.2.4 Sample AP5 Cu-MOF **(**RAMP 5′ HT 30′)

The sample was introduced into the microwave reactor and processed under the same programmed conditions as AP4 but with blank carbon. A bigger magnetic stir bar was placed into the solution to ensure uniform mixing. The temperature gradually rose to 120 °C for RAMP of 5 minutes and maintained for a hold time of 30 minutes (Fig.3.2.4). The maximum operational limits were again set at 250 W power and 250 psi (≈17.2 bar) pressure, although the actual values recorded during the run were much lower.

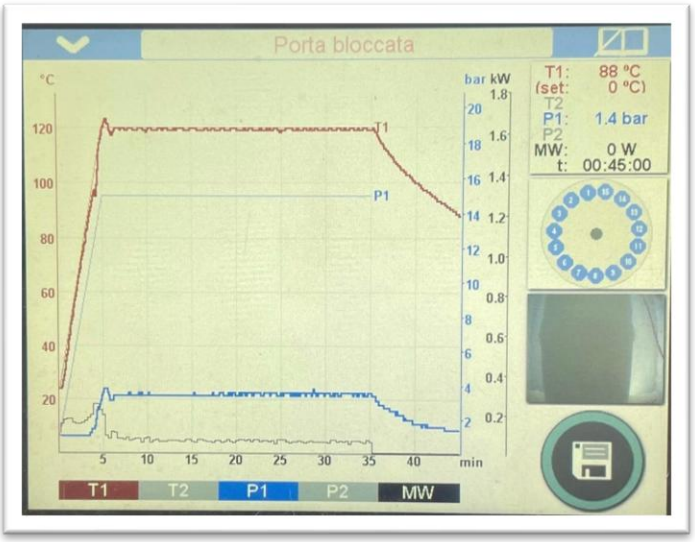

Figure 3.2.4: Microwave reactor control panel during synthesis of AP5 Cu-MOF **(**RAMP 5′ HT 30′)

The system data show that the pressure stabilized around 3.4-3.6 bar (Tab.3.2.4). After the completion of the hold period, the reactor was cooled and the final product solution was obtained under these controlled synthesis conditions. After microwave-assisted synthesis the final product solution was collected from the reactor.

Table 3.2.4: Microwave control panel during synthesis of AP5 Cu-MOF **(**RAMP 5′ HT 30′)

Time	**Pressure** **bar**	**Temperature** **°C**	**Power** **W**
6:04 s	3.4	118	108
16:21 s	3.6	120	63
25:04 s	3.4	120	64
35:00 s	3.6	120	0
45:00 s	1.4	88	0

3.2.5 Sample AP6 Cu-MOF/Vulcan Carbon **(**RAMP 20′ HT 5′)

The sample was placed in the microwave reactor and subjected to the programmed synthesis conditions. A bigger magnetic stir bar was introduced into the solution to ensure uniform mixing. The temperature gradually increased to 120 °C for RAMP of 20 minutes and maintained for a hold time of 5 minutes (Fig.3.2.5). Throughout the process, the maximum limits of 250 W power and 250 psi (≈17.2 bar) pressure were set, but the actual operating values remained significantly lower. The recorded data show that the maximum pressure stabilized at around 3.8 bar, while the applied microwave power fluctuated between 57-80 W to sustain the reaction temperature (Table.3.2.5). After the completion of the hold period, the reactor cooled naturally and the final product solution of final product was obtained under these controlled conditions.

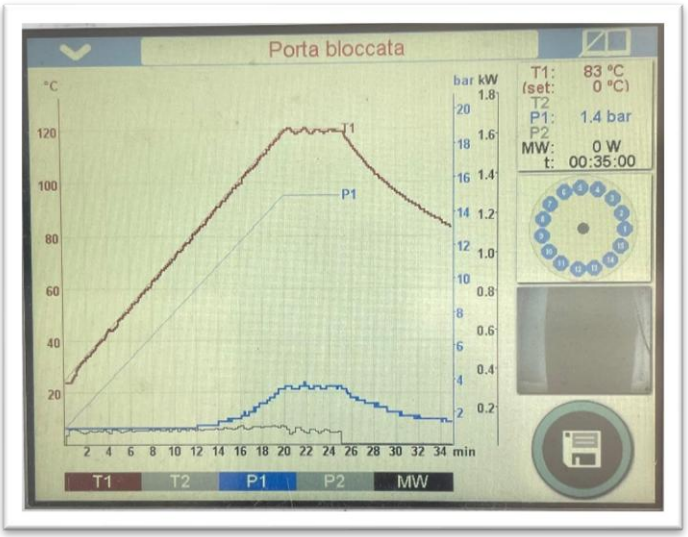

Figure 3.2.5: Microwave reactor control panel during synthesis of AP6 Cu-MOF/Vulcan Carbon **(**RAMP 20′ HT 5′)

Remember that when pressure drops up to 1 bar, we can open the microwave. After microwave-assisted synthesis the final product solution was collected from the reactor.

Table 3.2.5: Microwave control panel during synthesis of AP6 Cu-MOF/Vulcan Carbon **(**RAMP 20′ HT 5′)

Time	**Pressure bar**	**Temperature °C**	**Power W**
5:06 s	1.0	49	57
10:03 s	1.0	72	80
16:39 s	2.0	104	74
20:49 s	3.4	120	60
25:00 s	3.4	120	0
30:02 s	2.0	97	0
35:00 s	1.4	83	0

3.2.6 Sample AP9 Cu-MOF/Mesoporous Carbon **(**RAMP 5′ HT 30′)

The sample was placed in the microwave reactor and subjected to the programmed synthesis conditions. A small magnetic stir bar was introduced into the solution to ensure uniform mixing. The temperature gradually increased to 120 °C for RAMP of 5 minutes and maintained for a hold time of 30 minutes (Fig.3.2.6). Throughout the process, the maximum limits of 250 W power and 250 psi (≈17.2 bar) pressure were set, but the actual operating values remained significantly lower. The recorded data show that the maximum pressure stabilized at around 3.6 bar, while the applied microwave power fluctuated between 74-86 W to sustain the reaction temperature (Table.3.2.6). After the completion of the hold period, the reactor cooled naturally and the final product solution was obtained under these controlled conditions.

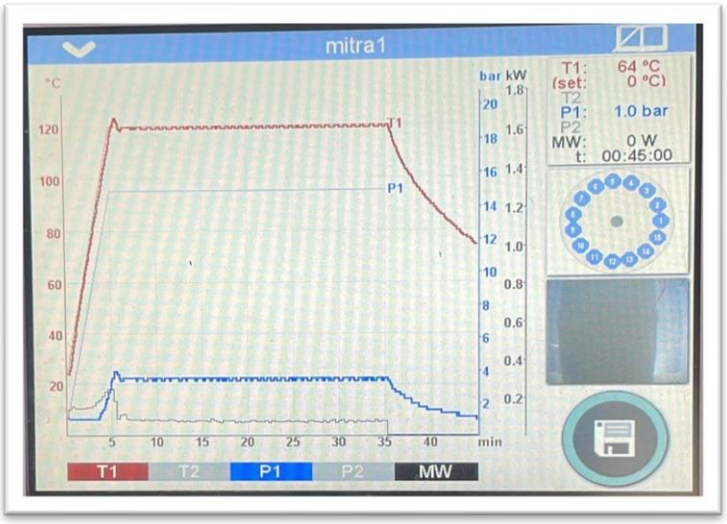

Figure 3.2.6: Microwave reactor control panel during synthesis of AP9 Cu-MOF/Mesoporous Carbon **(**RAMP 5′ HT 30′)

Rember that when pressure drops up to 1 bar, we can open the microwave. After microwave-assisted synthesis the final product solution was collected from the reactor.

Table 3.2.6: Microwave control panel during synthesis of AP9 Cu-MOF/Mesoporous Carbon **(**RAMP 5′ HT 30′)

Time	**Pressure bar**	**Temperature °C**	**Power W**
6:38 s	3.6	120	86
15:18 s	3.6	120	77
26:05 s	3.6	120	74
35:56 s	2.9	113	0
45:00 s	1	64	0

3.3 Autoclave assisted synthesis

3.3.1 Sample AP7 AP8 synthesis (Cu-MOF/Vulcan carbon)

After the preparation of the AP7 Cu-MOF/Vulcan Carbon and AP8 Cu-MOF/Vulcan Carbon precursor solutions, each mixture was carefully transferred into a Teflon-lined stainless-steel autoclave reactor. Once the precursor solutions were loaded, the autoclave was tightly sealed to create a closed and pressure-resistant system capable of withstanding elevated temperature and pressure conditions generated during the solvothermal reaction. The sealed autoclaves were then placed in a Thermo-Scientific oven and subjected to heating at 120 °C for a duration of 3 hours (Fig.3.3.1).

Figure 3.3.1: Thermo-scientific oven heated autoclave system

Upon completion of the heating cycle, the oven was turned off, and the autoclaves were allowed to cool naturally to room temperature inside the oven. Natural cooling was preferred to prevent sudden pressure drops or thermal shocks. Once cooled, the autoclaves were carefully opened, and the resulting suspensions were collected for further post-synthesis treatment such as washing, filtration, and drying to obtain the final MOF materials.

Table 3.3.1: Thermo-scientific oven parameters

Sample	Temperature	Hold Time
AP7 Copper -MOF/ Vulcan carbon	120 °C	3 hours
AP8 Copper -MOF/ Vulcan carbon	120 °C	3 hours

3.4 Centrifugation and washing

Immediately after collection, each sample product solution was subjected to centrifugation to separate the solid fraction from the liquid.

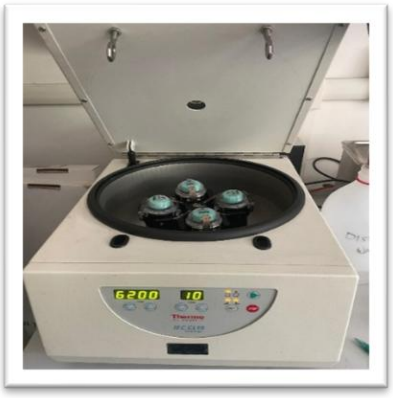

Figure 3.4: Thermo-Scientific IEC CL10 Centrifuge

After centrifugation, the precipitated products were subjected to washing to remove impurities. AP1 Cu-MOF (RAMP 20′ HT 30′) and AP7 Cu-MOF/Vulcan Carbon were washed with a solvent of 10ml mixture consisting of 90% DI water and 10% ethanol. Whereas all other samples were washed with 10ml solvent mixture consisting of 50% DI water and 50% ethanol (Table.3.4). Sample AP8 Cu-MOF/Vulcan Carbon was not subjected to any washing step.

Table 3.4: Centrifugation parameters for purification and separation

Sample	RPM	Hold Time(minutes)	Washing cycle
AP1 Cu-MOF (RAMP 20′ HT 30′)	6200	5′	Once
AP3 Cu-MOF/Vulcan carbon (RAMP 20′ HT 30′)	6200	5′	Twice
AP4 Cu-MOF/Vulcan carbon (RAMP 5′ HT 30′)	6200	5′	Twice
AP5 Cu-MOF (RAMP 5′ HT 30′)	6200	10′	Once
AP6 Cu-MOF/Vulcan carbon (RAMP 20′ HT 5′)	6200	10′	Once
AP7 Cu-MOF/Vulcan carbon	6200	5′	Once
AP8 Cu-MOF/Vulcan carbon	6200	5′	No wash
AP9 Cu-MOF/Mesoporous carbon (RAMP 5′ HT 30′)	6200	10′	Twice

3.5 Drying process

All the samples were dried using a Buchi Glass Oven, a precision-controlled laboratory drying unit designed for vacuum drying of materials at moderate temperatures (Fig.3.5). The drying process was carried out under reduced pressure to ensure gentle removal of residual solvents and moisture without thermal degradation. Sample was placed in the oven's glass chamber, and the temperature and hold time were adjusted. While sample AP8 Cu-MOF/Vulcan carbon was dried by using thermos-scientific oven (Fig.3.3).

Figure 3.5: BUCHI Glass Oven B-585

Table 3.5: Summary of drying conditions and final yield product

Sample	Temperature °C	Hold Time (hours)	Equipment	Final product weight
AP1 Cu -MOF (RAMP 20′ HT 30′)	80	12	Buchi	113 mg
AP3 Cu -MOF/ Vulcan carbon (RAMP 20′ HT 30′)	80	16	Buchi	380 mg
AP4 Cu -MOF/ Vulcan carbon (RAMP 5′ HT 30′)	80	18	Buchi	520 mg
AP5 Cu -MOF (RAMP 5′ HT 30′)	80	16	Buchi	157 mg
AP6 Cu -MOF/ Vulcan carbon (RAMP 20′ HT 5′)	80	16	Buchi	337 mg
AP7 Cu -MOF/ Vulcan carbon	80	18	Buchi	327 mg
AP8 Cu -MOF Vulcan carbon	80	14	Thermo-scientific oven	335 mg
AP9 Cu -MOF/ Mesoporous carbon (RAMP 5′ HT 30′)	80	18	Buchi	235 mg

3.6 Structural and morphological characterization

3.6.1 X-Ray Diffractometry Analysis

X-ray diffraction is a wide, non-destructive, and versatile technique used for the study of crystal structures and their atomic interatomic spacing. The main principle behind this is the constructive interference of monochromatic X-rays. The latter are generated using a cathode ray tube, filtered to generate monochromatic radiation, and then directed towards the crystalline sample to be analyzed. [17] As these X-rays interact with the orderly array of atoms within the crystal lattice, constructive interference occurs under specific conditions defined by Bragg's Law. This law dictates the precise relationship between the incident X-ray wavelength, the atomic spacing within the crystal, and the angles at which diffracted beams emerge from the sample.

$$n\lambda = 2dsin(\theta) \qquad (3.6.1)$$

Where n is an integer number, λ is the X-rays wavelength, d is the interplanar spacing generating the diffraction, and θ is the diffraction angle. The diffracted rays are then detected, counted and thus, by scanning the sample through a 2θ angles range, it is possible to understand all the possible diffraction directions of the lattice. Nevertheless, by converting the measured diffraction peaks into d-spacings, one can identify the compound present in the sample. This identification relies on the unique fingerprint of d-spacings associated with each crystalline material. Typically, the obtained d-spacings are compared against established reference databases containing patterns for known compounds. The equipment consists of an X-ray tube which produces beams, a sample holder, and a X-ray detector as illustrated in Fig.3.6.1. [17] The X-rays are generated by heating up a metal filament to produce electrons and subsequently accelerating them to bombard a target material. When electrons have sufficient energy to dislodge inner shell electrons of the target material, characteristic X-ray spectra are produced, with specific wavelengths typical of the target material Cu, Fe, Cr, etc.. The experiment

involves rotating both the sample and the detector to record the intensity of the reflected X-rays. This process allows for the identification of specific crystallographic planes within the sample. When the geometry between the incident X-rays and the crystal lattice satisfies Bragg's Law, constructive interference occurs, resulting in a sharp peak in the recorded intensity. As it can be seen in the image, the sample rotates in the path of the collimated beam at an angle equal to θ, while the detector is placed on an arm to collect the diffracted X-rays and rotates at an angle of 2θ.

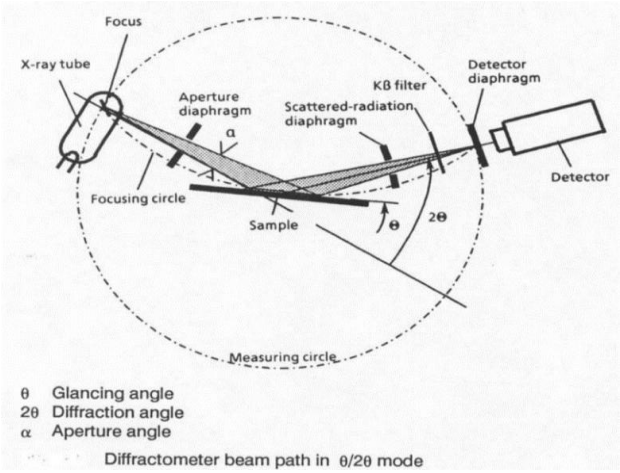

Figure 3.6.1. Schematic diagram of a diffractometer system. [17]

X-ray diffraction measurements were performed using a PANalytical X'Pert PRO diffractometer (Fig.3.6.1A). The system was used to determine the crystalline phases and structural characteristics of the prepared nanostructured materials.

Figure 3.6.1B: Sample holder preparation for XRD

The powdered catalyst sample was first placed in a clean eppendorf tube after drying. A small quantity of the powder was carefully transferred into the sample holder and levelled gently using a glass slide (Fig.3.6.1B). The preparation aimed to ensure uniform X-ray reflection and minimize surface irregularities. The holder was then mounted on the goniometer stage inside the XRD instrument ensuring precise alignment for accurate measurement.

Table 3.6.1: XRD operating program

Parameter	value
Start angle (2θ)	5°
End angle (2θ)	60°
Step size	0.0262606°
Number of steps	2034
Time per step	200.175 s
Net time per step	197.115 s
Total scan time	29.08 min
Scan speed	0.03343°/s
Operating current	40 mA
Operating power	40 kW

Once the sample was properly leveled, the holder was securely mounted on the goniometer stage inside the instrument (Fig.3.6.1A). Precise alignment of the sample surface with the incident X-ray beam was ensured to maintain consistent geometry during measurement. All measurements were performed under controlled conditions (Tab.3.6.1).

Figure 3.6.1A: PANalytical X'Pert PRO diffractometer

3.6.2 Field Emission Scanning Electron Microscope

According to Leng [18], the scanning electron microscope is the most widely utilized type of electron microscope due to its versatility and non-destructive nature, providing detailed information about the morphology and composition of a specimen. It enables the analysis of microscopic structures by scanning the surface of materials with a focused electron beam, achieving high resolution and significant depth of field, which results in images with a three-dimensional appearance.

During operation, the interaction between the incident electron beam and the specimen's atoms occurs through both elastic and inelastic scattering processes, producing different types of signals. In elastic interactions, the kinetic energy of the electrons remains unchanged, while inelastic scattering involves energy transfer from the electron beam to the specimen's atoms, generating electrons with reduced energy and minor trajectory deviations. These signals provide valuable information about the topography, surface features, and elemental composition of the analyzed specimen.

A typical scanning electron microscope consists of an electron gun which generates a stable and intense electron beam, a series of electromagnetic lenses and apertures that focus and direct the beam onto the specimen's surface, and a positively charged grid that attracts the emitted electrons toward the detector (Fig. 3.6.2). The electron beam is usually produced by a thermionic electron gun, in which a filament (cathode) commonly made of tungsten or lanthanum hexaboride is heated by an electrical current. When the filament reaches a sufficiently high temperature, its work function is overcome, allowing electrons to escape and form the beam. However, thermionic emitters have several operational drawbacks, including cathode material evaporation, relatively low brightness, thermal drift during operation, and surface charging of the specimen.

To overcome these limitations and obtain higher-resolution images, Field Emission Scanning Electron Microscopy is employed. It utilizes a field emission gun, also known as a cold cathode emitter, which emits electrons without heating the filament. Instead, electron emission is achieved by applying a very high electric potential gradient to the filament. The filament is typically a tungsten wire sharpened to a fine tip approximately 100 nm, which reduces the work function of the cathode and facilitates efficient electron emission.

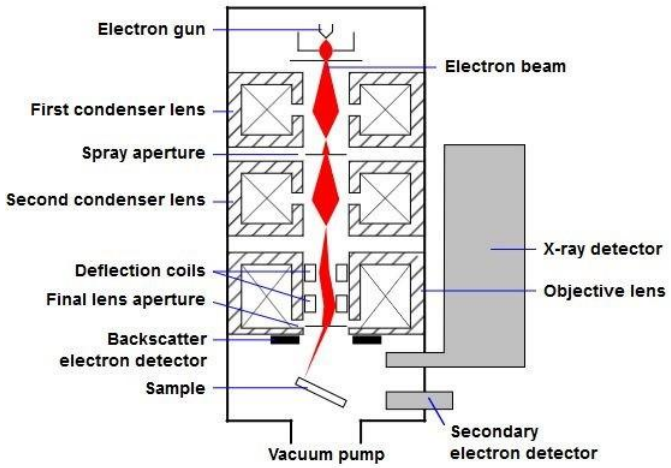

Figure 3.6.2: A schematic representation of a SEM [©User:Steff, modified by User:ARTE / Wiki- media Commons / CC-BY-SA-3.0].

It produces cleaner images with minimal electrostatic distortion and offers spatial resolution up to six times higher than that of conventional scanning electron microscope. Both operate under vacuum

conditions to minimize electron scattering and interference, ensuring clearer and more accurate imaging.

3.7 Selection and assembly of electrolytic cell

The electrolytic cell plays a critical and often decisive role in determining the performance of electrochemical carbon dioxide reduction catalysts. Its operation involves several interdisciplinary aspects, including fluid mechanics, structural mechanics, chemical mass transfer, and electronic engineering. However, researchers generally place greater emphasis on studying the materials, catalysts, and fundamental scientific mechanisms of electrochemical carbon dioxide reduction, while paying less attention to engineering innovations in electrolytic cell design. Consequently, the development of electrolytic cells has progressed relatively slowly. Currently, three main types of electrolytic cells are commonly employed in laboratory research: the H-cell, the flow-cell, and the membrane electrode assembly cell (Fig.3.7) [19].

However, the H-cell has two major drawbacks. First, because of the very low solubility of carbon dioxide in the electrolyte, mass transfer of carbon dioxide within the cell is significantly limited, leading to slow electrochemical carbon dioxide reduction kinetics. Second, only neutral electrolytes can be used in this setup. In alkaline electrolytes, carbon dioxide reacts with hydroxide ions to form carbonate salts, while in acidic electrolytes, the hydrogen evolution reaction becomes strongly favoured, suppressing the desired reduction process. Despite these limitations such as slow reaction kinetics and high energy consumption the H-cell remains widely used for fundamental studies due to its simple design and ease of operation (Fig.3.7 A).

In the flow-cell, the gas diffusion electrode is designed so that one side is exposed to the incoming carbon dioxide gas, while the other side is in contact with the electrolyte. This arrangement enables the simultaneous presence and interaction of three phases gas, liquid, and solid corresponding to carbon dioxide, electrolyte, and catalyst, respectively (Fig.3.7 B).

The membrane electrode assembly electrolytic cell is considered highly suitable from an industrial standpoint (Fig. 3.7 C). In this configuration, both the anode and cathode are placed in direct contact with opposite sides of an ion-exchange membrane, forming a compact sandwich like structure without separate compartments. This design minimizes ohmic losses by significantly reducing the distance between the two electrodes. During operation, carbon dioxide is continuously supplied to the cathode, while the anode is typically fed with an electrolyte solution such as potassium bicarbonate, potassium hydroxide, or water to facilitate the oxygen evolution reaction. Since the catholyte is eliminated [20] in this configuration, ion transport occurs primarily through the ionomer layers and the membrane itself.

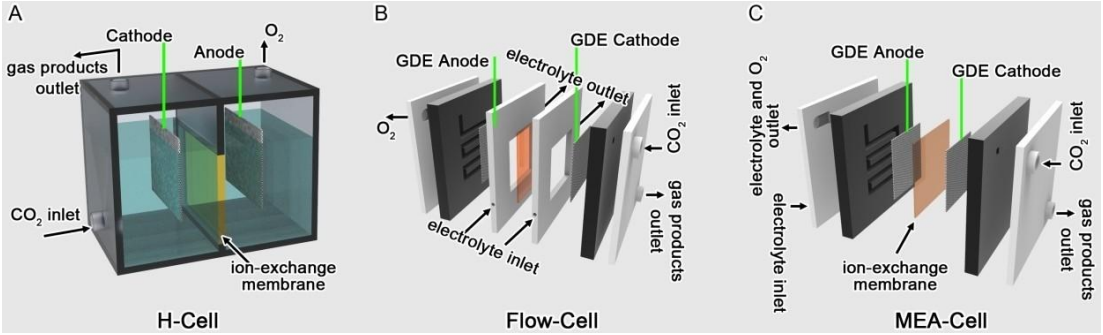

Figure 3.7 [19].: (A) H-cell (B) flow-cell and (C) MEA-cell configurations

3.7.1 Materials used

For each sample four electrodes were prepared in total using 15.18 cm² carbon paper with a gas diffusion layer. A total of 32 mg of the synthesized Cu-based catalyst was used, corresponding to 8 mg per electrode. 170.7 µL Nafion and 2000 µL isopropyl alcohol were used to prepare the catalyst ink which was uniformly applied onto the carbon paper and dried at room temperature. The total loading corresponded to 1.6 mg/cm² of catalyst on each electrode.

3.7.2 Electrode preparation

Firstly 32 mg of the synthesized Cu-based catalyst was dispersed in 2000 µL of isopropyl alcohol (IPA) and sonicated for 10 minutes to obtain a uniform suspension. Then, 170.7 µL of Nafion was added as a binder to enhance the adhesion of the catalyst to the carbon paper, followed by an additional 30 minutes of sonication for complete homogenization. After preparing the catalyst ink a 15.18 cm² piece of carbon paper was used as the substrate. The ink was drop-cast uniformly over the surface and allowed to dry at room temperature. Once dried, the coated carbon paper was cut into three equal electrodes each with a length and width of 2.25 cm × 2.25 cm, corresponding to an active area of 5.06 cm² (Fig.3.7.2).

Figure 3.7.2: Fabrication of Cu-based catalyst electrodes with a loading of 1.6 mg/cm²

3.7.3 Electrolyte preparation

A 0.5 M potassium hydroxide (KOH) electrolyte solution was prepared by dissolving the 28.055 g of KOH pellets in 1000 mL of deionized (DI) water. The mixture was placed on a magnetic stirrer and stirred continuously until the KOH was completely dissolved, forming a clear and homogeneous solution. The prepared 0.5 M KOH solution was then used as the electrolyte for all electrochemical experiments.

3.8 Electrochemical characterization

Electrochemical Impedance Spectroscopy is a technique used to analyze systems where ionic conduction dominates over electronic conduction, such as in the presence of electrolytes. In this method, alternating current voltage is applied to the electrochemical system, and the corresponding current response is measured. The experiment can be performed using either a two-electrode or a three-electrode configuration [21].

Although electrochemical systems are inherently non-linear, a pseudo-linear approximation is generally valid when the amplitude of the applied alternating current voltage is kept sufficiently small. In this context, the applied sinusoidal voltage can be expressed as $V(\omega, t) = V_0 \sin(\omega t)$, where V_0represents the amplitude of the signal and $\omega = 2\pi f$is the angular frequency corresponding to the

chosen frequency f. The measured current response, $I(\omega, t)$, occurs at the same frequency.
This system's characteristic behavior is known as resistors, capacitors, and inductors the theoretical relationships can be derived accordingly. The impedance (Z) of the system is then defined as the ratio between the applied voltage and the resulting current.

$$\mathrm{Z}(\omega, \mathrm{t}) = \frac{\mathrm{V}(\omega, \mathrm{t})}{\mathrm{I}(\omega, \mathrm{t})}$$

Chronopotentiometry is an electrochemical technique used to study reaction mechanisms and kinetics. In this method, a constant current is applied for a specific period, while the potential of the working electrode is measured and recorded as a function of time. When the experiment begins, redox-active species diffuse toward the working electrode to balance the applied electron current. This process continues until the concentration of the redox species (diffusion-limited condition) becomes zero at the electrode surface.

$$O + ne^- \rightleftharpoons R \qquad (3.8.1)$$

Considering the general equation (3.8.1), when the concentration of Oat the electrode surface becomes zero, the potential of the electrode shifts toward more negative values, reaching a transient time τ. The transient time has an analytical relationship with the diffusion coefficient and the concentration of species O:

$$\tau^{3/2} = \frac{2C_0^* nFAD_0^{1/2}}{3\beta} \qquad (3.8.2)$$

where $C_0^*$is the bulk concentration of O, n is the number of electrons transferred, $F$is Faraday's constant, A is the working electrode area, $D_0$is the diffusion coefficient, and $\beta$is the sweep rate equation (3.8.2).

3.9 Product characterization

Gas Chromatography is a widely used analytical technique for separating and analyzing gaseous compounds. As described by Regmi and Agah [22], it operates based on the physical principle of differential migration of gas mixture components as they pass through a column containing a stationary phase. This setup is illustrated in Figure 3.9. At the outlet of the column, a detector measures the quantity of each separate component over time. The time difference between the sample injection and the detection of a specific component indicated by the peak maximum in the chromatogram is referred to as the total retention time t_R of that component.

Furthermore, the difference between the total retention time t_R and the hold-up time t_M the time a component spends in the mobile phase, which is identical for all components is defined as the adjusted retention time t'_R. This value represents the actual time the component remains in the stationary phase.

$$t'_R = t_R - t_M \qquad (3.9)$$

The retention factor depends on the strength of interaction between a component and the stationary phase. A higher retention factor indicates stronger interaction and, consequently, a longer retention time. The value of k is also influenced by the column temperature, generally decreasing as the temperature increases. Another key parameter is the average linear velocity ū of the mobile phase. Due to the non-uniform pressure distribution along the column, the mobile phase exhibits a velocity gradient throughout its length.

$$\bar{u} = \frac{L}{t_M} \qquad (3.9.1)$$

Here, L represents the column length, and t_M denotes the retention time of an unretained component methane is commonly used as the unretained marker compound. The average linear velocity significantly affects the separation efficiency of the column and, consequently, the overall resolution of the chromatographic process. Various physical and chemical processes occurring within the column, along with additional factors such as injection pulse width and dead volumes, collectively influence the separation and dispersion of the components. These combined effects determine the shape and resolution of the chromatogram obtained from the injected sample.

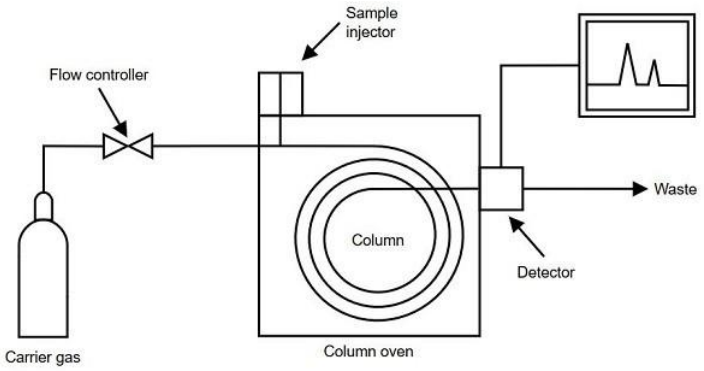

Figure 3.9: Typical GC configuration. The carrier gas is used to control the flow of the injected sample [Wikimedia Commons public domain image].

4- RESULTS AND DISCUSSION

In this chapter, the morphological, structural, and electrochemical characterization results of all the synthesized materials are presented and discussed in detail. The first section focuses on the analysis of the morphology and chemical composition of each synthesized material individually, highlighting their distinctive structural and compositional features. In the subsequent section, the electrochemical performance of the fabricated electrodes is examined, with measurements carried out under various applied potentials.

4.1 Field emission scanning electron microscopy

4.1.1 Sample AP1 Cu-MOF (RAMP 20′ HT 30′)

The sample generally exhibits an evenly distributed surface morphology. The material displays a combination of rounded and nearly spindle shape crystal structures (Figure 4.1.1).

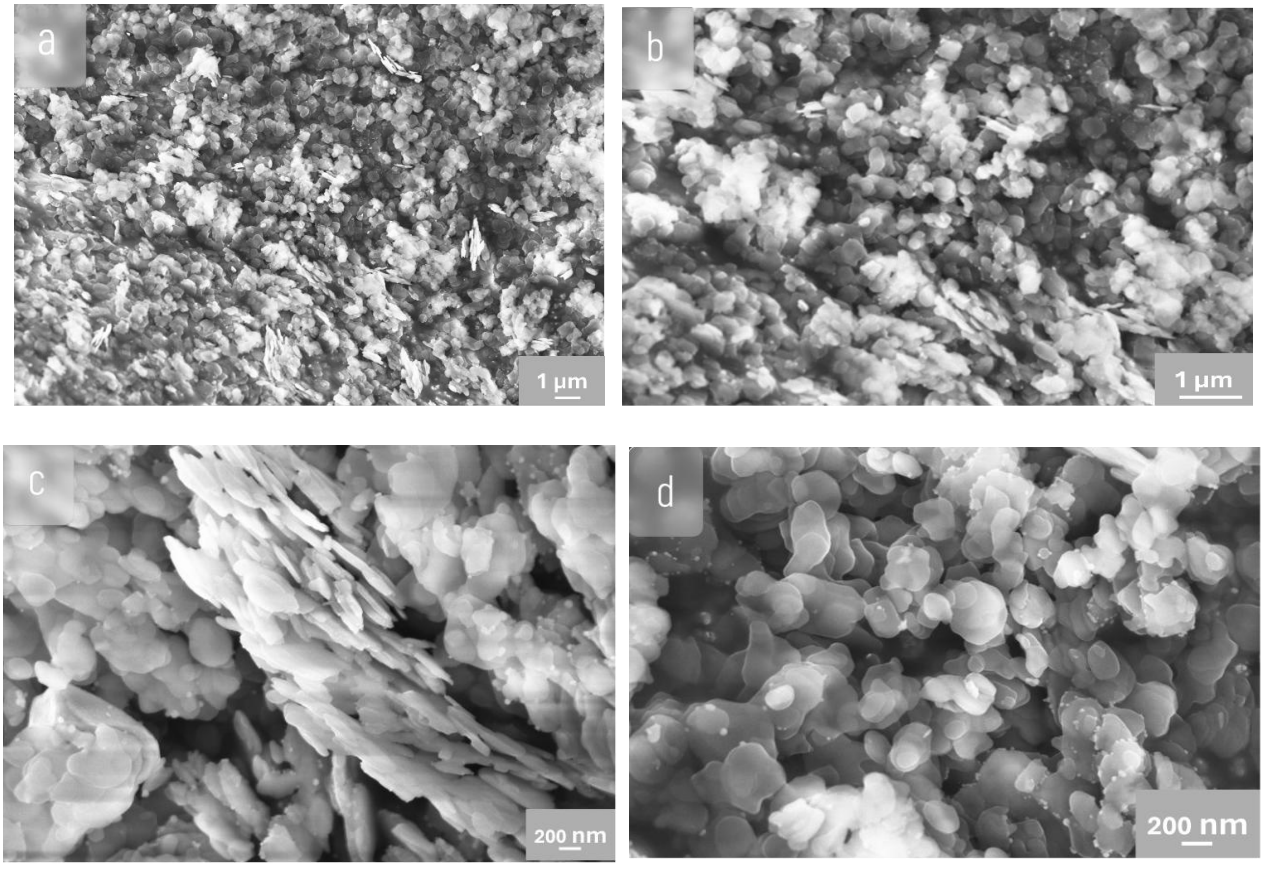

Figure 4.1.1: Field emission scanning electron microscopy images of the sample AP1 Cu-MOF with magnification value 500 Kx (a) 1000 Kx (b) 2500 Kx (c) 2500 Kx (d).

4.1.2 Sample AP3 Cu-MOF/Vulcan carbon (RAMP 20′ HT 30′)

The images reveal that the sample possesses an unclear grain boundary (Figure 4.1.2). While the surface with Vulcan carbon is significantly rougher than the pure Cu-MOF AP1 (RAMP 5′ HT 30′) indicating that the Vulcan carbon has been successfully attached to the surface of Cu-MOF.

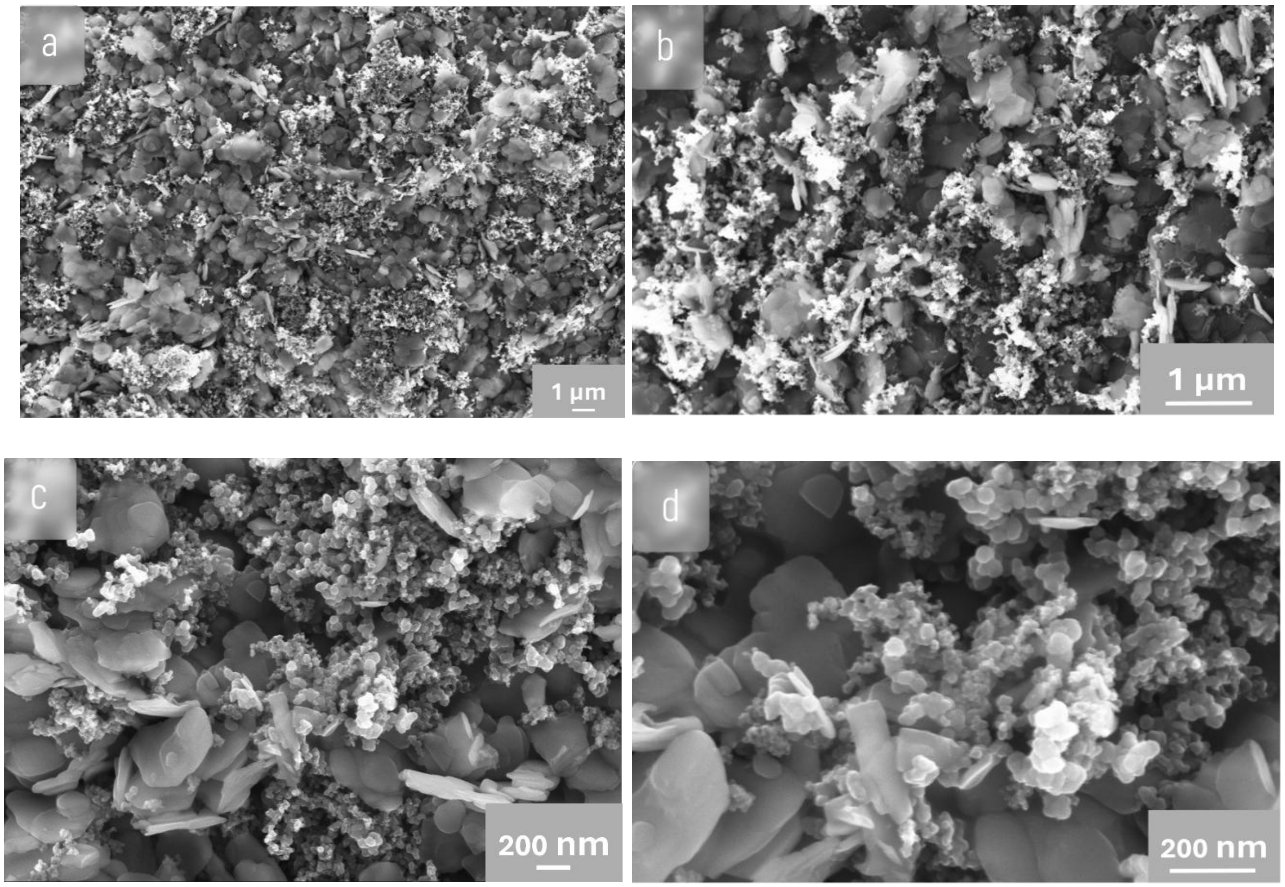

Figure 4.1.2: Field emission scanning electron microscopy images of the sample AP3 Cu-MOF/Vulcan Carbon **(**RAMP 20′ HT 30′) with magnification value 500 Kx (a) 1000 Kx (b) 2500 Kx (c) 5000 Kx (d).

4.1.3 Sample AP4 Cu-MOF/Vulcan carbon **(**RAMP 5′ HT 30′)

The material showed a combination of rod like and irregular crystal shapes with evenly distributed surface. Rough surface indicates Vulcan carbon has been successfully attached to the surface of Cu-MOF (Figure 4.1.3).

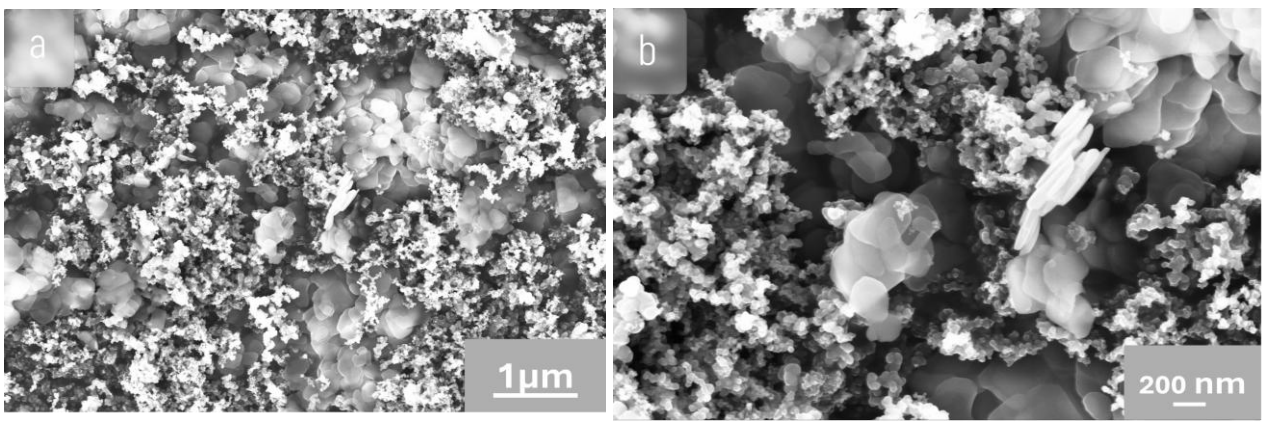

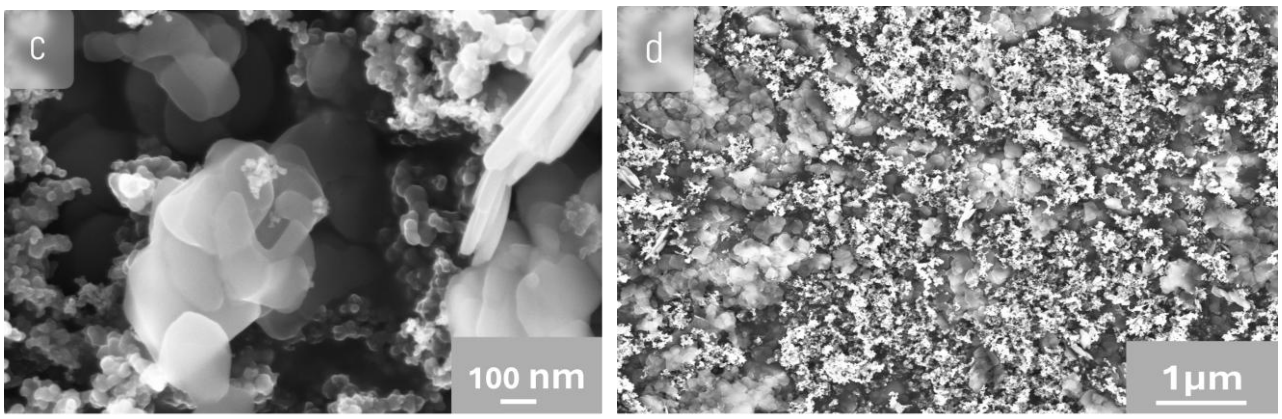

Figure 4.1.3: Field emission scanning electron microscopy images of the sample AP4 Cu-MOF/Vulcan Carbon **(**RAMP 5′ HT 30′) with magnification value 1000 Kx (a) 2500 Kx (b) 5000 Kx (c) 500 Kx (d).

4.1.4 Sample AP5 Cu-MOF **(**RAMP 5′ HT 30′)

The sample exhibits an evenly distributed surface morphology with irregular shapes crystals (Figure 4.1.4).

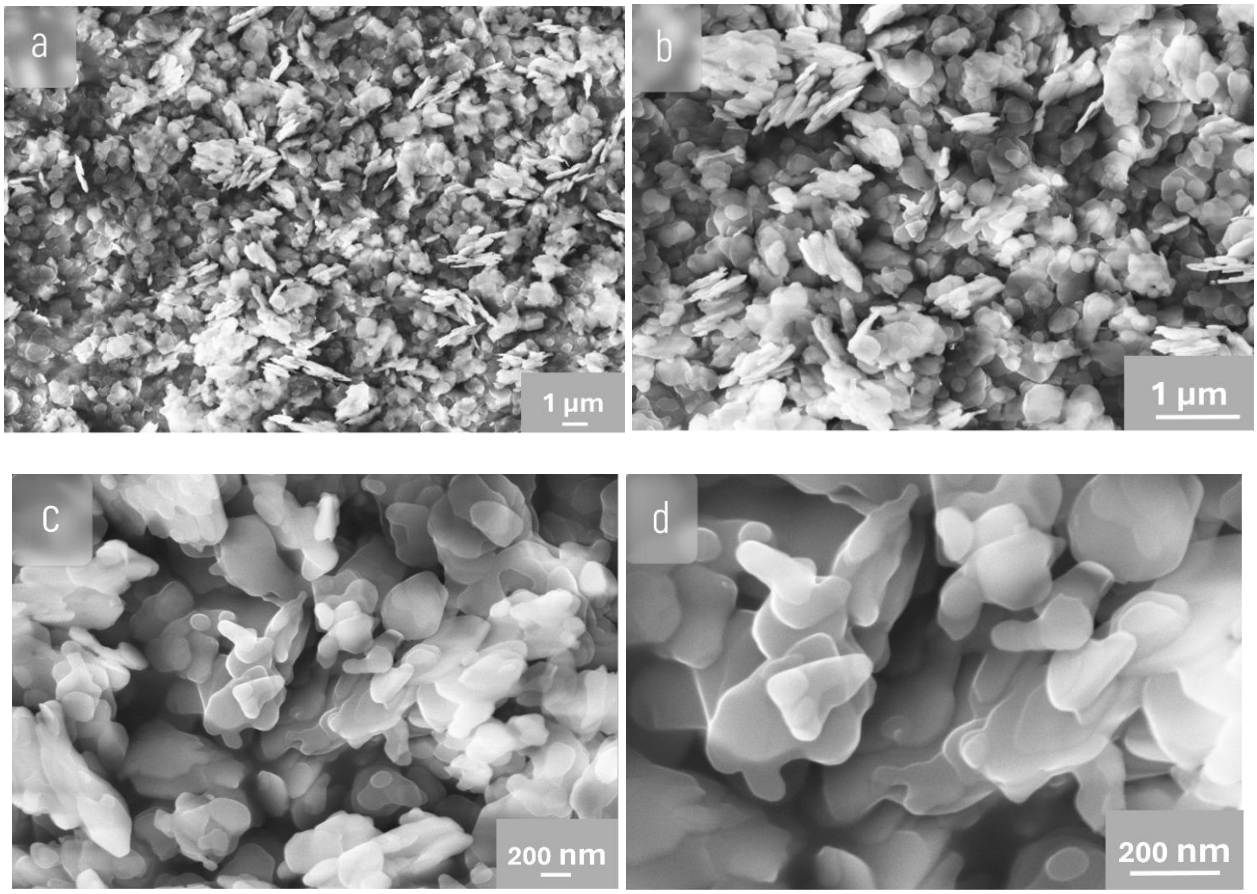

Figure 4.1.4: Field emission scanning electron microscopy images of the sample AP5 Cu-MOF **(**RAMP 5′ HT 30′) with magnification value 500 Kx (a) 1000 Kx (b) 2500 Kx (c) 5000 Kx (d).

4.1.5 Sample AP6 Cu-MOF/Vulcan carbon (RAMP 20′ HT 5′)

The morphology of the synthesized material is not well defined showing irregular and poorly resolved structures (Figure 4.1.5).

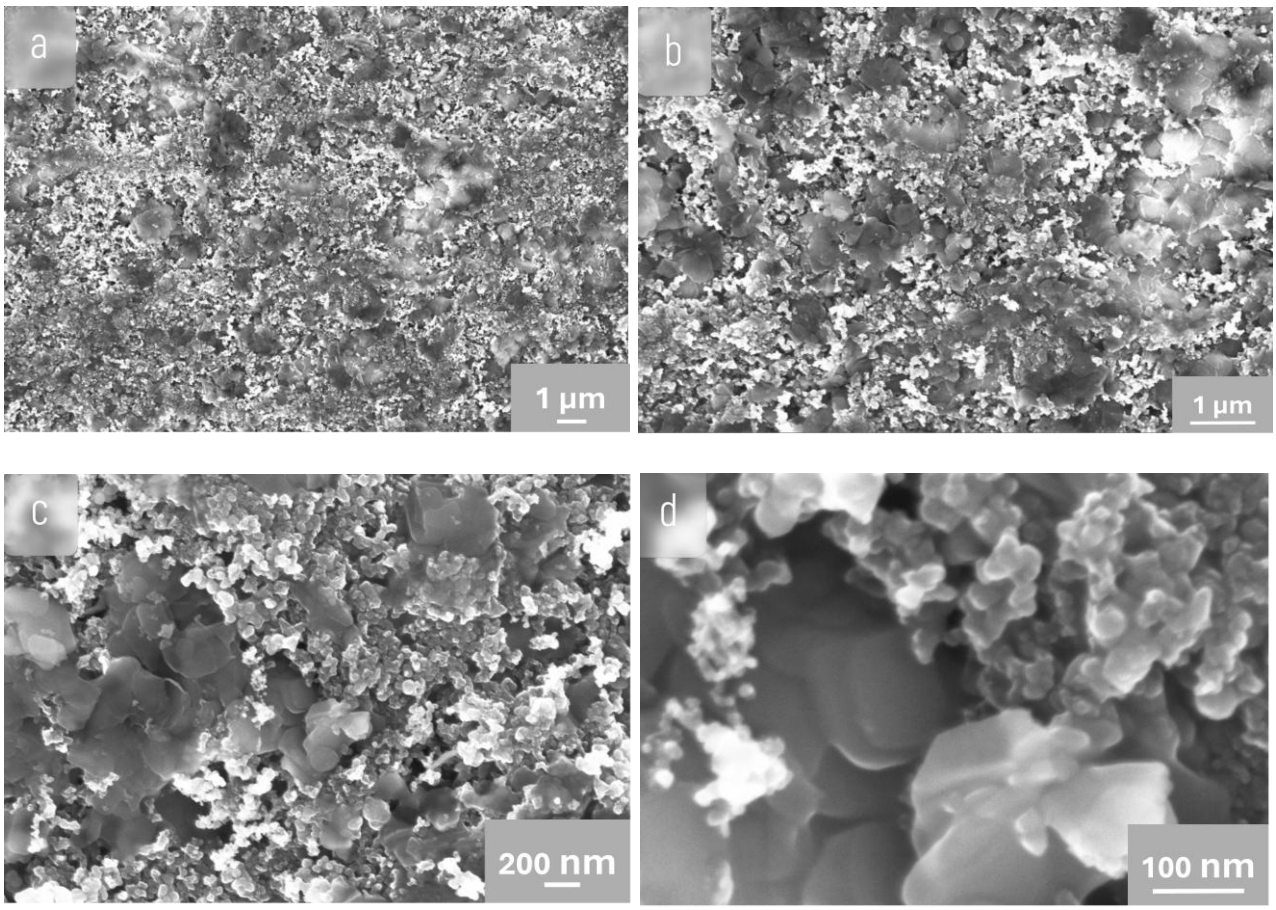

Figure 4.1.5: Field emission scanning electron microscopy images of the sample AP6 Cu-MOF/Vulcan Carbon (RAMP 20′ HT 5′) with magnification value 500 Kx (a) 1000 Kx (b) 2500 Kx (c) 10000 Kx (d).

4.1.6 Sample AP7 Cu-MOF/Vulcan carbon

No distinct or uniform particle shape was observed instead of the sample exhibits irregular and nonhomogeneous morphology and poorly extracted material crystals (Figure 4.1.6).

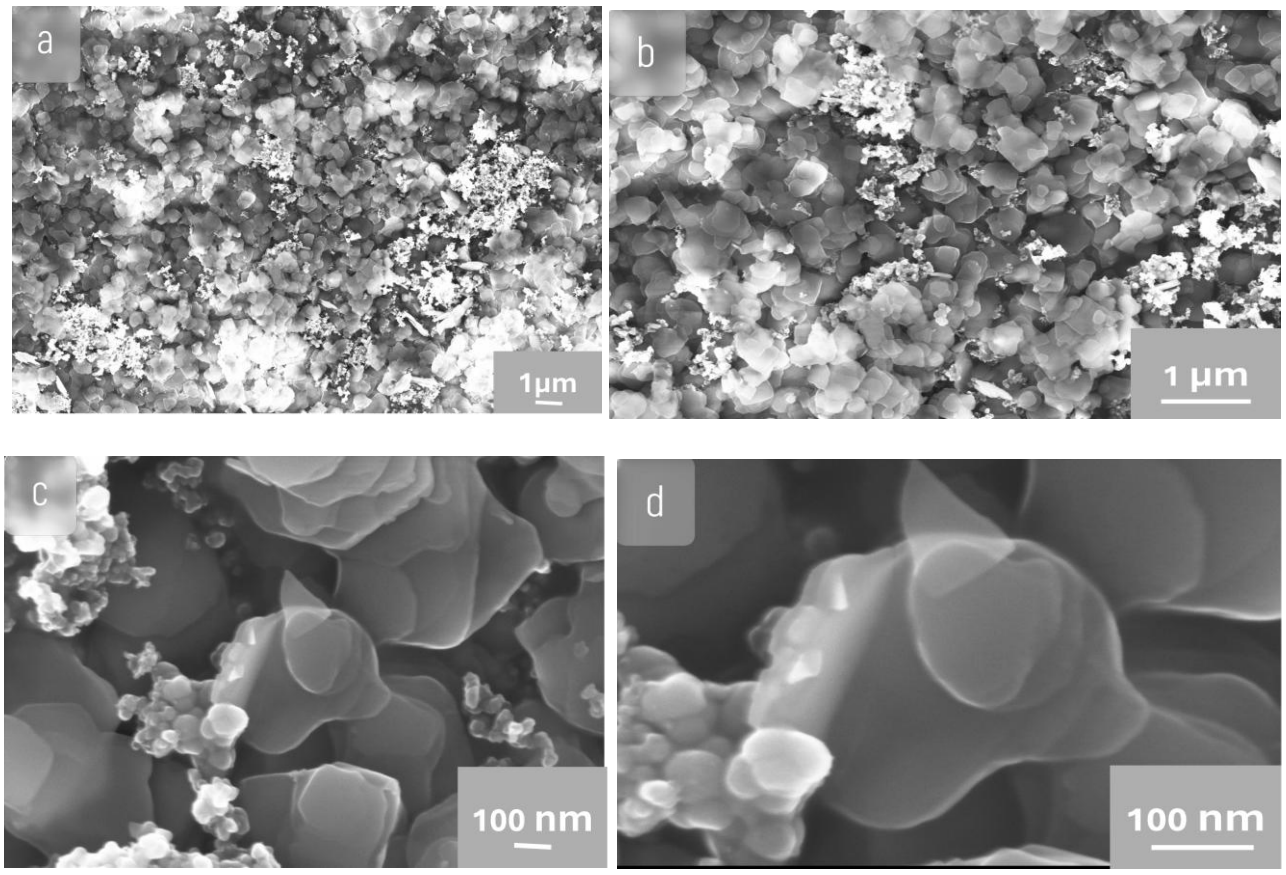

Figure 4.1.6: Field emission scanning electron microscopy images of the sample AP7 Cu-MOF/Vulcan Carbon with magnification value 500 Kx (a) 1000 Kx (b) 5000 Kx (c) 10000 Kx (d).

4.1.7 Sample AP8 Cu-MOF/Vulcan carbon

The sample displays a highly agglomerated and disordered morphology hindering clear visualization of the characteristic structural features of the material (Figure 4.1.7). Crystals not extracted well with non-uniform distribution.

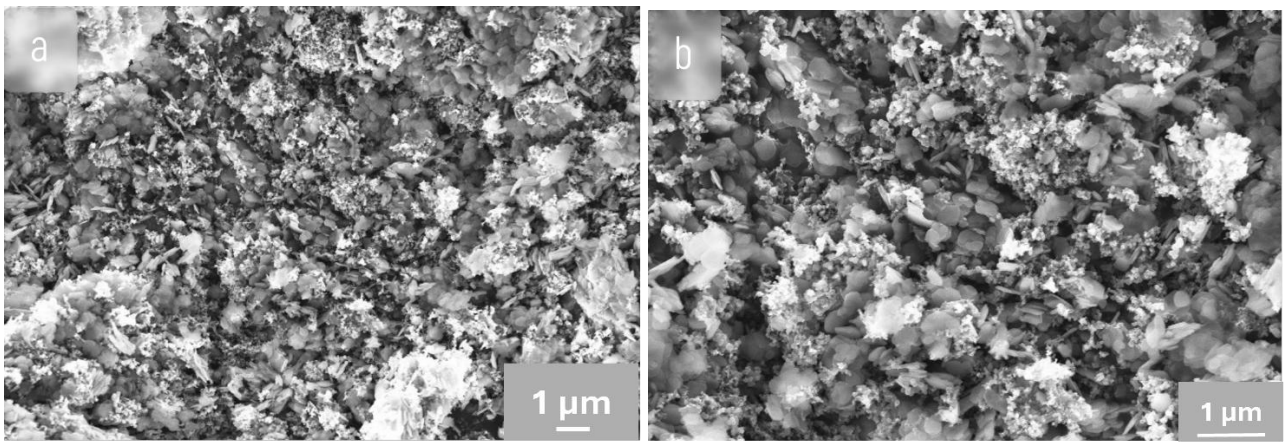

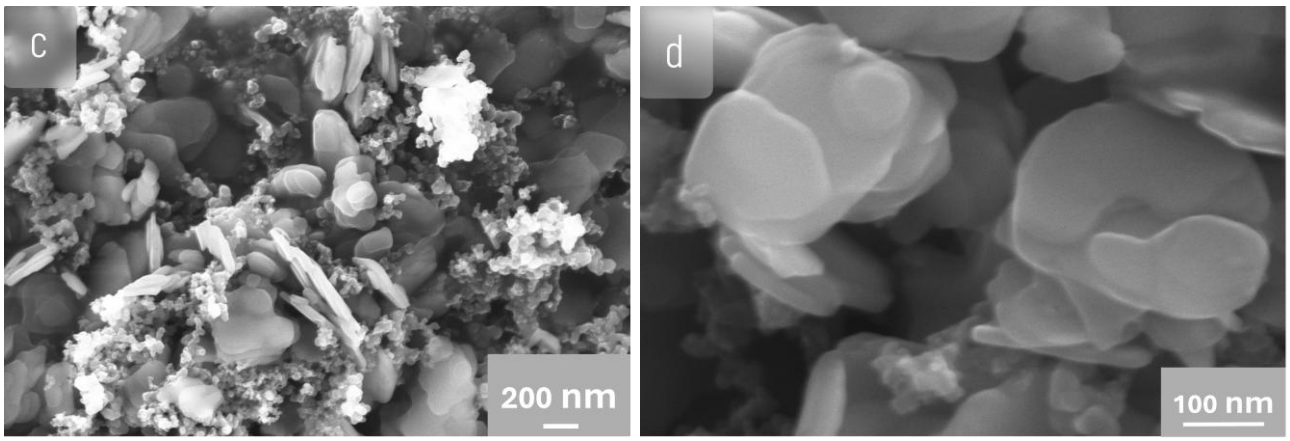

Figure 4.1.7: Field emission scanning electron microscopy images of the sample AP8 Cu-MOF/Vulcan Carbon with magnification value 500 Kx (a) 1000 Kx (b) 2500 Kx (c) 10000 Kx (d).

4.1.8 Sample AP9 Cu-MOF/Mesoporous carbon (RAMP 5′ HT 30′)

The sample showed densely packed uniformly distributed flower like structures with distinct geometric features compared to other synthesized samples (Figure 4.1.8).

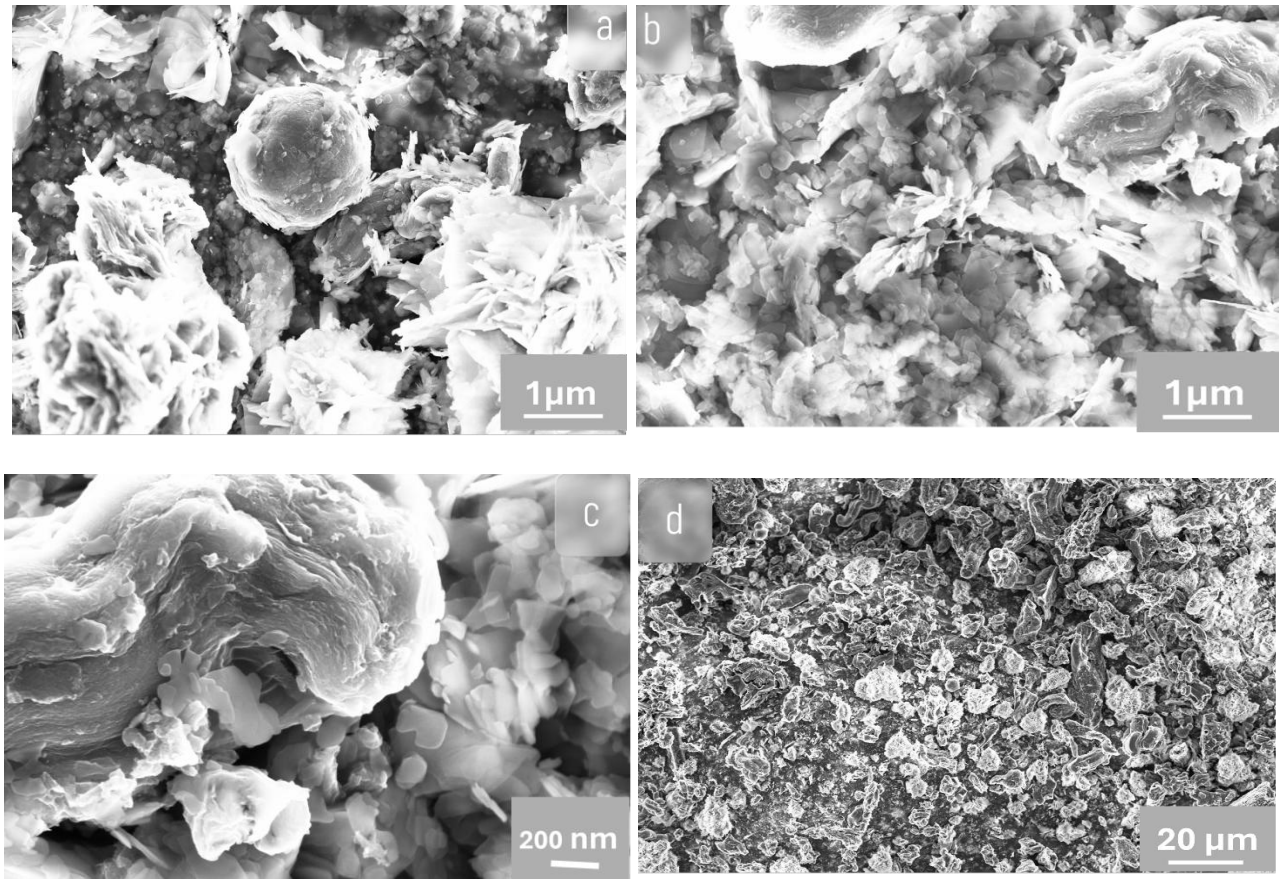

Figure 4.1.8: Field emission scanning electron microscopy images of the sample AP9 Cu-MOF/Mesoporous Carbon (RAMP 5′ HT 30′) with magnification value 500 Kx (a) 1000 Kx (b) 2500 Kx (c) 500 Kx (d).

4.2 XRD

It is one of the most important characterization techniques used to investigate the crystallographic structure, phase purity, and structural evolution of synthesized materials. In this study, XRD analysis was employed to examine the structural properties of the synthesized catalysts as well as to evaluate the influence of microwave synthesis parameters such as ramp time and hold time on crystal formation. The XRD patterns of the synthesized Cu-MOF samples exhibited well-defined diffraction peaks, confirming the crystalline nature of the framework.

The observed peaks match closely with the reported data [32] confirming phase purity and successful formation of the Cu-MOFs. Sharp and intense peaks suggest good crystallinity with minimal structural defects. The diffraction peaks of synthesized samples correspond to the characteristic planes of the Cu-MOF, consistent with previously reported Cu-based MOF structures. The XRD analysis also confirms that no secondary phases or impurities are present in the synthesized material.
This crystalline framework provides a high surface area and accessible active sites, making it promising for electrochemical reactions. Overall, the XRD results validate that the synthesized catalysts are structurally comparable to that reported in the literature and suitable for further experimental studies.

4.2.1 Sample AP1 Cu-MOF (RAMP 20′ HT 30′) and AP3 Cu-MOF/Vulcan carbon (RAMP 20′ HT 30′)

The characteristic diffraction peaks observed at 2θ = 14.6°, 29.6°, and 34.7° (Fig.4.2.1) correspond to the crystalline planes of Cu-MOF confirming its successful synthesis. Furthermore, a broad hump centered around ~15° in the 2θ range is evident, which can be attributed to the presence of Vulcan carbon in the AP3 Cu-MOF/Vulcan.

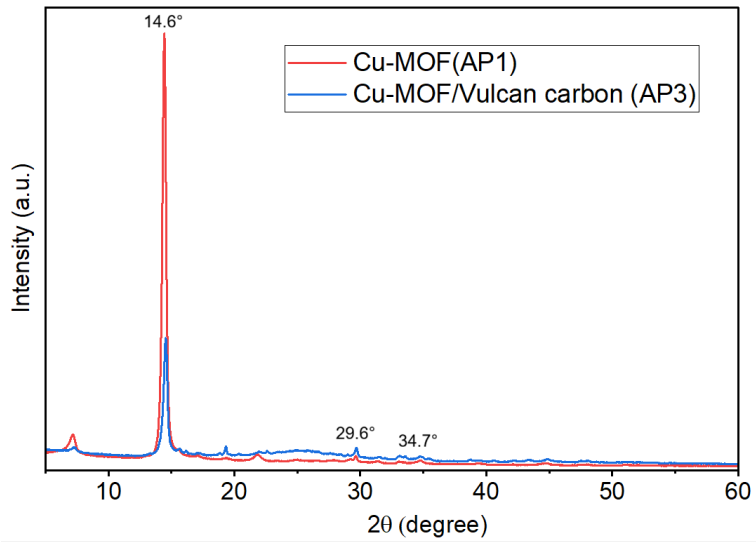

Figure 4.2.1. XRD AP3 Cu-MOF/Vulcan Carbon (RAMP 20′ HT 30′) and AP1 Cu-MOF (RAMP 20′ HT 30′)

4.2.2 Sample AP1 Cu-MOF(RAMP 20′ HT 30′) and AP5 Cu-MOF(RAMP 5′ HT 30′)

The diffraction peaks appeared at 2θ = 14.6°, 29.6°, and 34.7° (Fig.4.2.2) Based on these results, it can be presumably demonstrated that Cu-MOF was successfully synthesized. While lower RAMP significantly increased the intensity of all peaks.

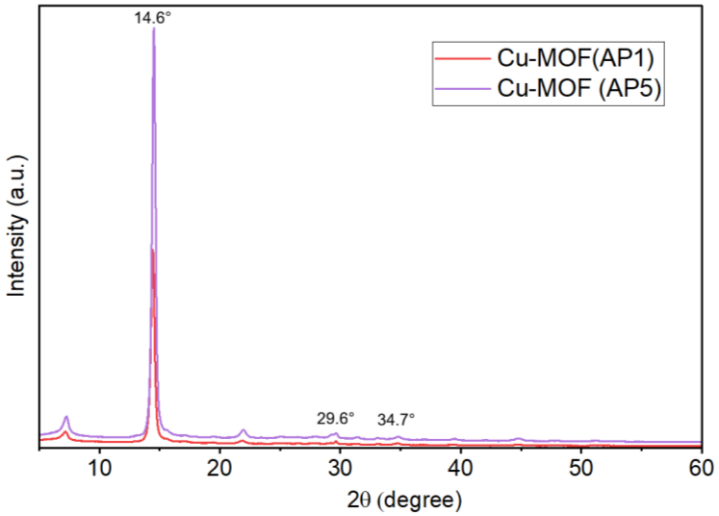

Figure 4.2.2. XRD AP1 Cu-MOF (RAMP 20′ HT 30′) and AP5 Cu-MOF (RAMP 5′ HT 30′)

4.2.3 Sample AP3 Cu-MOF/Vulcan carbon (RAMP 20′ HT 30′) and AP4 Cu-MOF/Vulcan carbon (RAMP 5′ HT 30′)

Prominent diffraction peaks appeared at 2θ = 14.6°, 29.6°, and 34.7° (Fig. 4.2.3) correspond to the crystalline planes of Cu-MOF. Additionally, the appearance of a hump near ~15° at 2θ signifies the presence of Vulcan carbon. Higher RAMP value lowers the intensity of 14.6° peak.

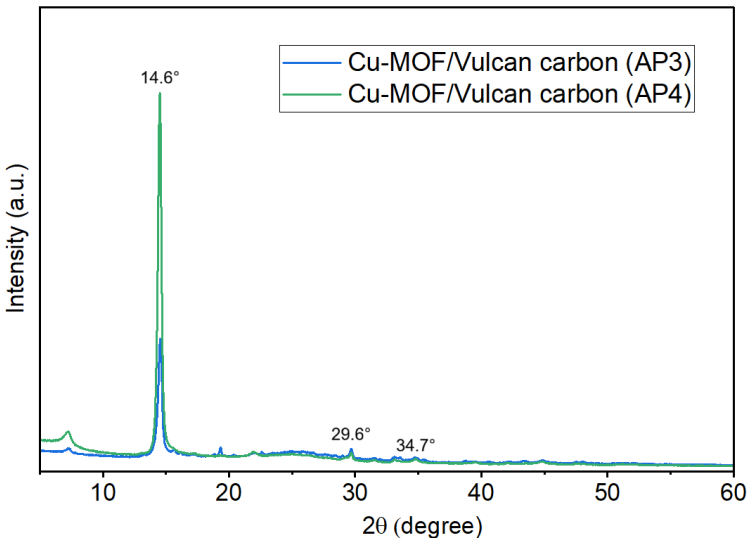

Figure 4.2.3. XRD AP3 Cu-MOF/Vulcan Carbon (RAMP 20′ HT 30′) and AP4 Cu-MOF/Vulcan Carbon (RAMP 5′ HT 30′)

4.2.4 **Sample AP3** Cu-MOF/Vulcan carbon **(**RAMP 20′ HT 30′) and **AP6** Cu-MOF/Vulcan carbon **(**RAMP 20′ HT 5′)

The characteristic diffraction peaks observed at 2θ = 14.6°, 29.6°, and 34.7° (Fig.4.2.4) correspond to the crystalline planes of Cu-MOF confirming its successful synthesis. Furthermore, a broad hump centered around ~15° in the 2θ range is evident, which can be attributed to the presence of Vulcan carbon. Lower hold time enhanced the intensity of all peaks.

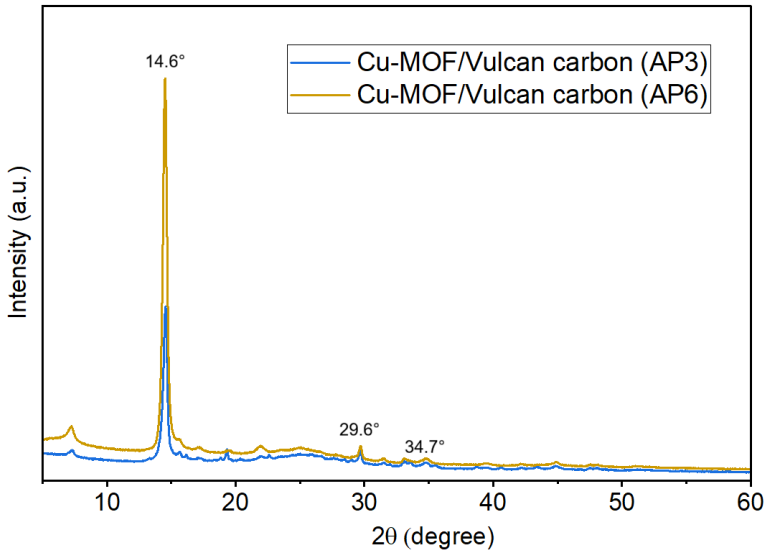

Figure 4.2.4. XRD AP3 Cu-MOF/Vulcan Carbon **(**RAMP 20′ HT 30′) and AP6 Cu-MOF/Vulcan Carbon **(**RAMP 20′ HT 5′)

4.2.5 **Sample AP4** Cu-MOF/Vulcan carbon **(**RAMP 5′ HT 30′) and **AP5** Cu-MOF **(**RAMP 5′ HT 30′)

The diffraction peaks appeared at 2θ = 14.6°, 29.6°, and 34.7° (Fig.4.2.5) Based on these results, it can be presumably demonstrated that Cu-MOF was successfully synthesized. While presence of Vulcan carbon in Cu-MOF significantly decreased the intensity of all peaks.

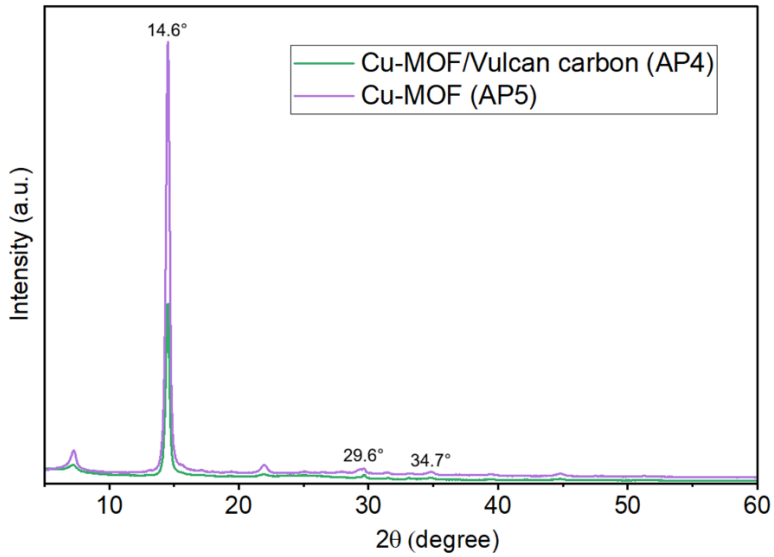

Figure 4.2.5. XRD AP4 Cu-MOF/Vulcan Carbon (RAMP 5′ HT 30′) and AP5 Cu-MOF (RAMP 5′ HT 30′)

4.3 Electrochemical Analysis

4.3.1 **AP1** Cu-MOF (RAMP 20′ HT 30′)

Electrochemical measurements were performed using five independently prepared electrodes with same material. The gas chromatography data demonstrated enhanced C_2H_4 selectivity up to 40% at 200 and 300 mA cm $^{-2}$, while at 50 mA cm^{-2} the product distribution shifted toward CO achieving 30% selectivity (Figure 4.3.1A). Linear sweep voltammetry measurements were conducted at specific applied potential on five electrodes of the same catalyst material slight variations in current density were observed among the electrodes (Figure 4.3.1C). These deviations may be attributed to minor differences in catalyst loading, ink dispersion, coating thickness, and electrode substrate contact during fabrication. Electrode potential curves over time at different applied current densities are demonstrated (Figure 4.3.1B).

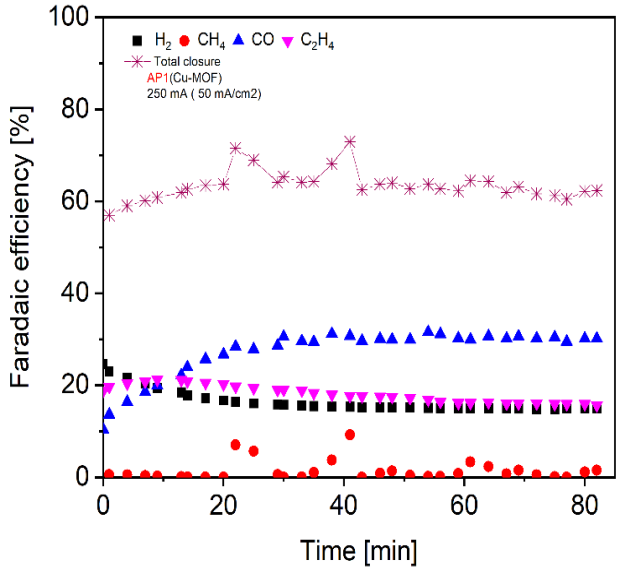

(a)

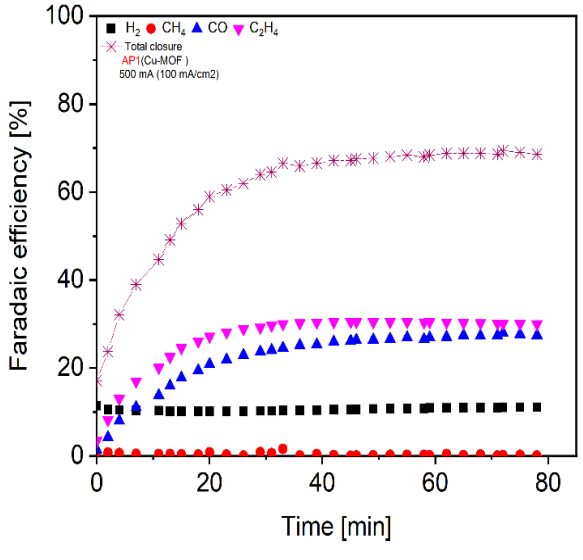

(b)

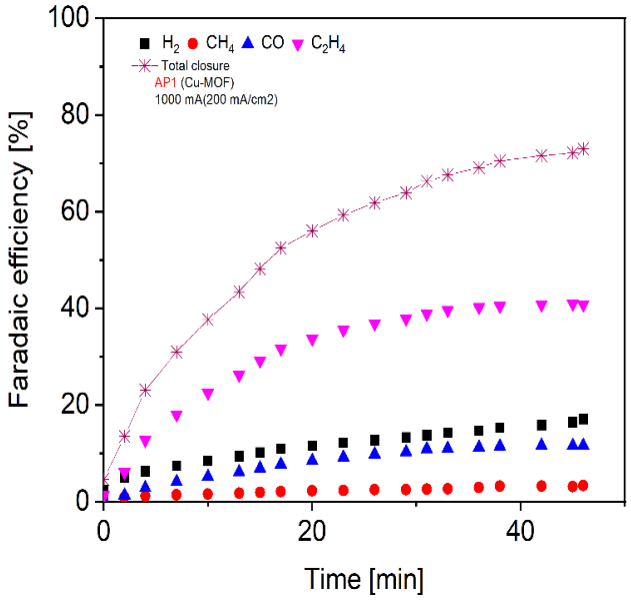

(c)

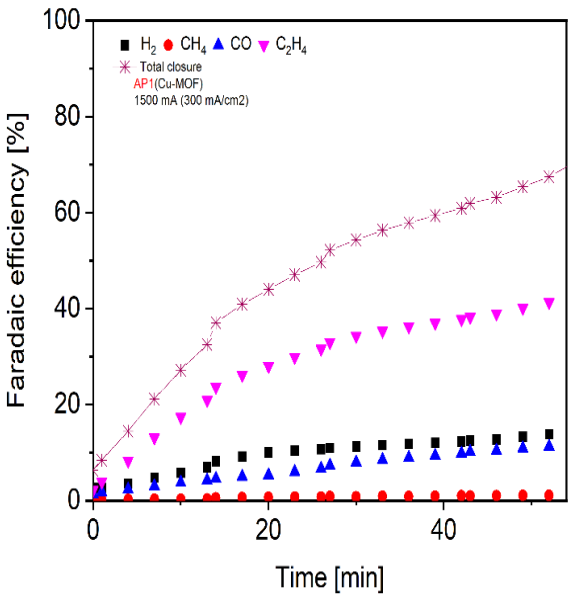

(d)

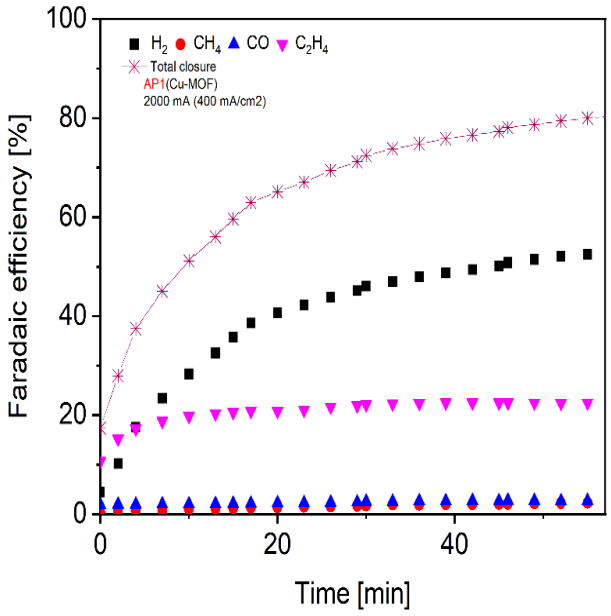

(e)

Figure 4.3.1. Evolution of faradaic efficiencies of gaseous products at constant applied current density (a) 50 mA/cm^2 (b) and 100 mA/cm^2 (c) 200 mA/cm^2 (d) and 300 mA/cm^2 (e) 400 mA/cm^2

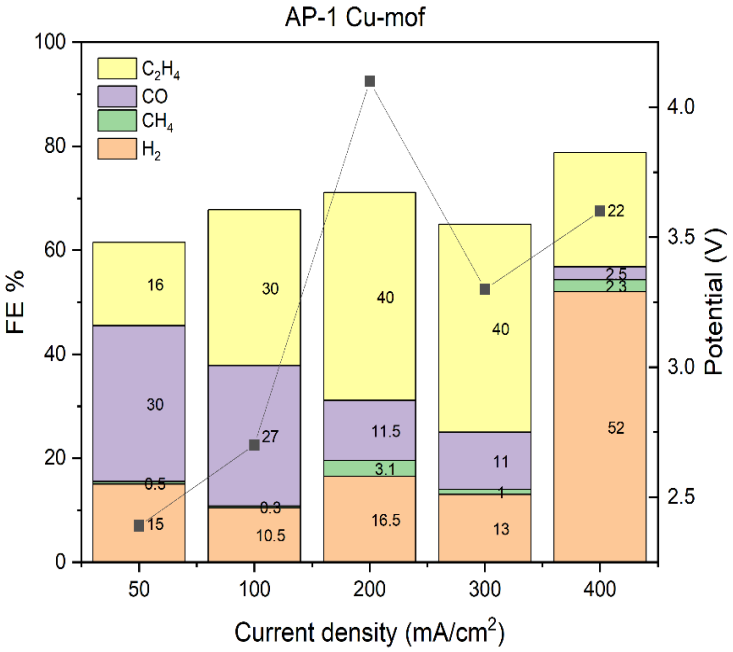

Figure 4.3.1A. Comparison of faradaic efficiencies of gaseous products at constant applied current densities.

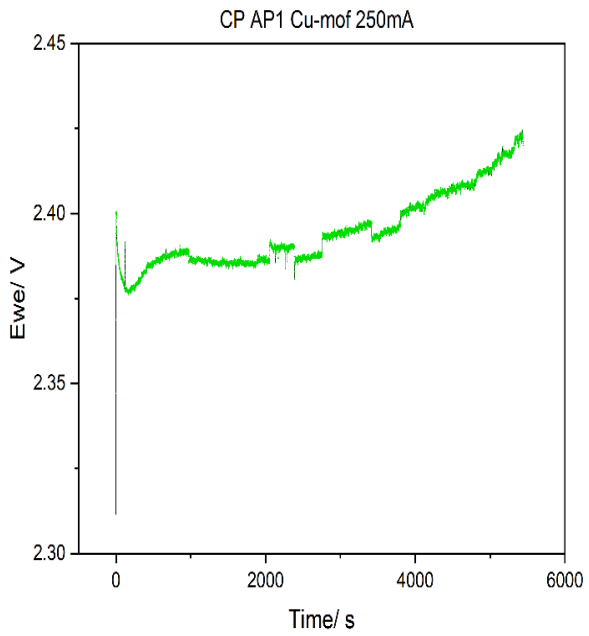

(a)

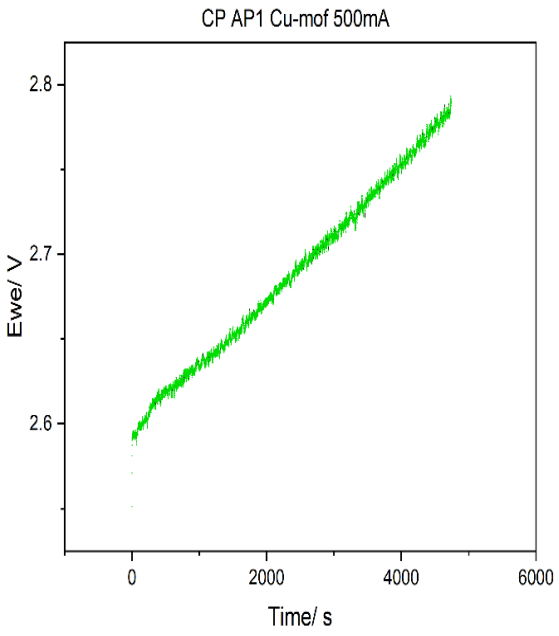

(b)

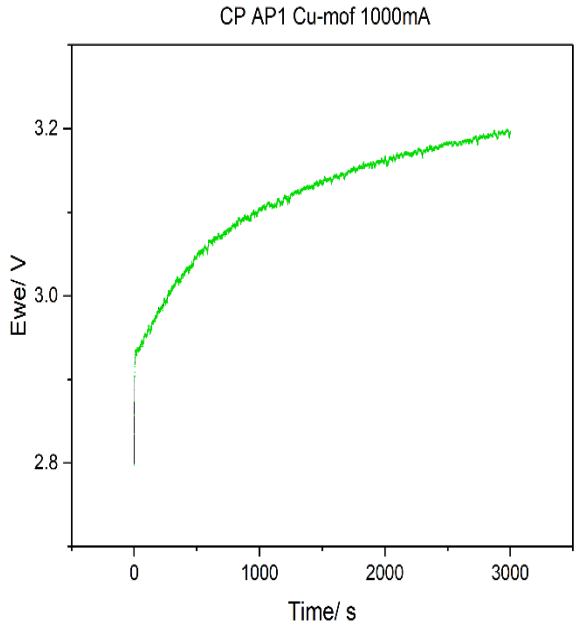

(c)

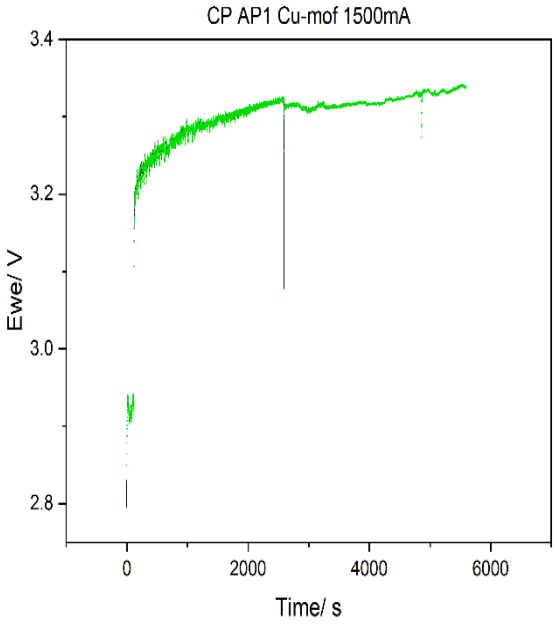

(d)

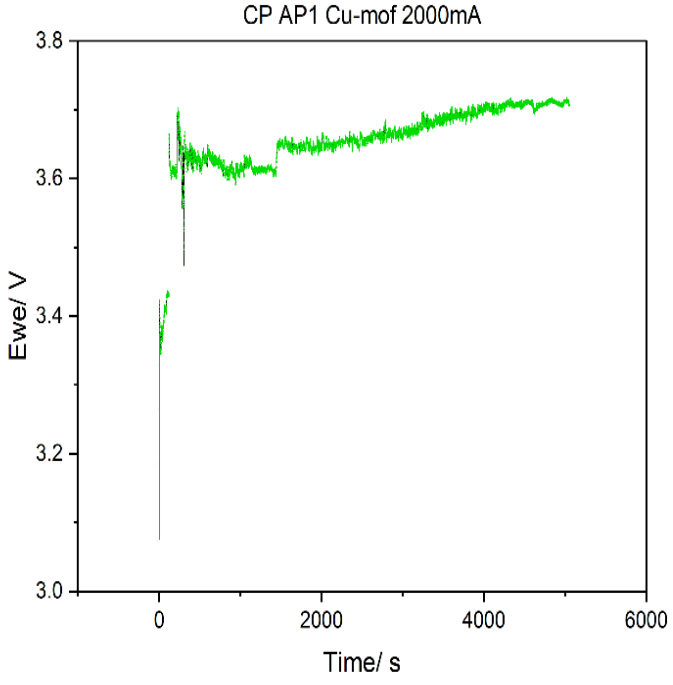

(e)

Figure 4.3.1B. Electrode potential curves over time at constant applied current densities (a) 50 mA/cm^2 (b) 100 mA/cm^2 (c) 200 mA/cm^2 (d) 300 mA/cm^2 (e) 400 mA/cm^2

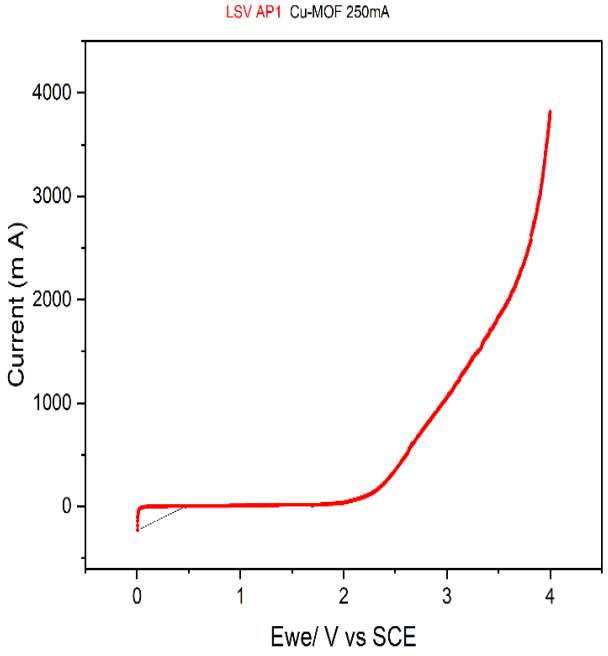
LSV AP1 Cu-MOF 250mA
Current (m A)
Ewe/ V vs SCE
4000
3000
2000
1000
0
0
1
2
3
4

(a)

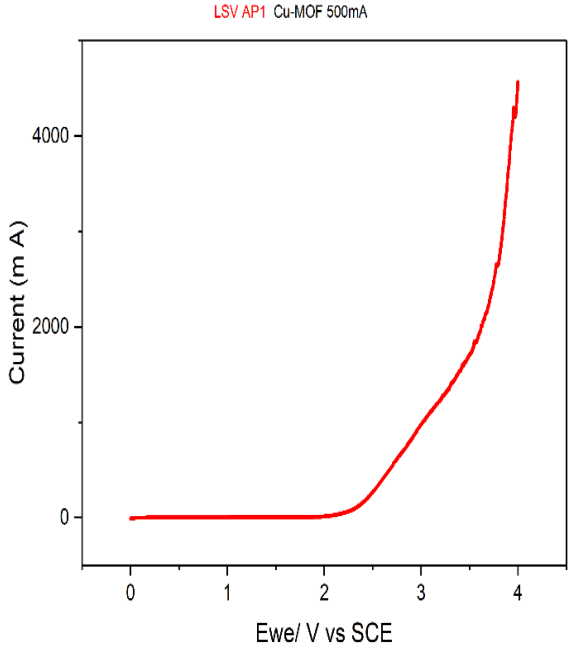
LSV AP1 Cu-MOF 500mA
Current (m A)
Ewe/ V vs SCE
4000
2000
0
0
1
2
3
4

(b)

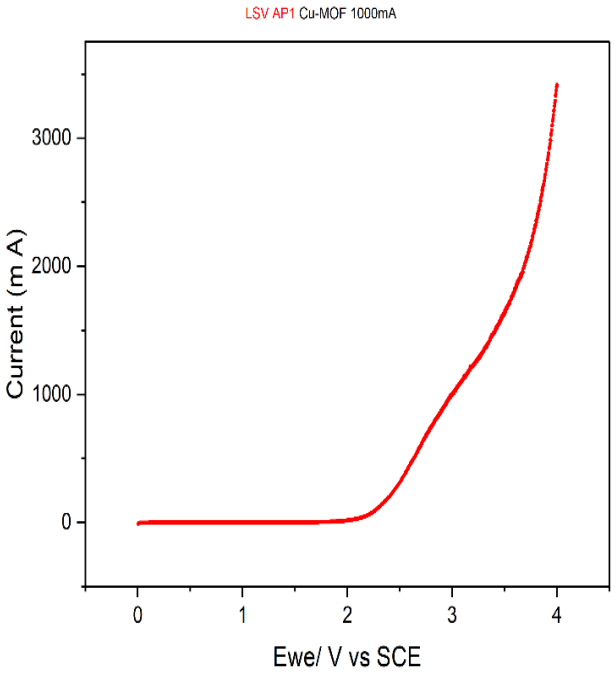
LSV AP1 Cu-MOF 1000mA
Current (m A)
Ewe/ V vs SCE
3000
2000
1000
0
0
1
2
3
4

(c)

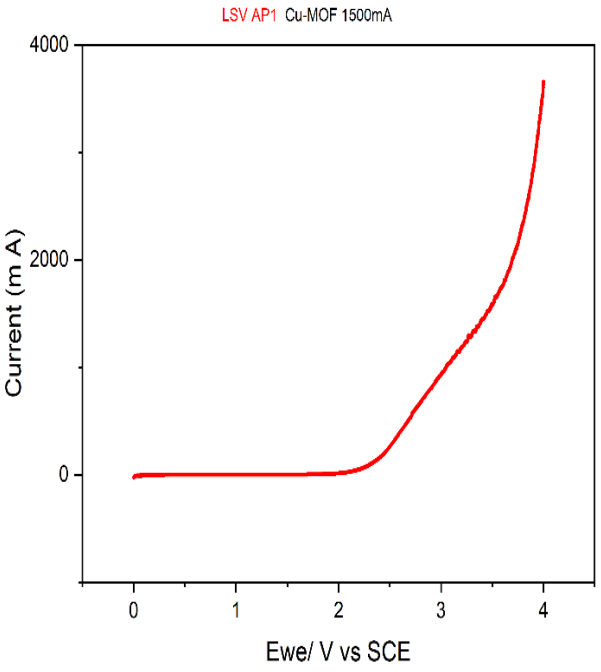
LSV AP1 Cu-MOF 1500mA
Current (m A)
Ewe/ V vs SCE
4000
2000
0
0
1
2
3
4

(d)

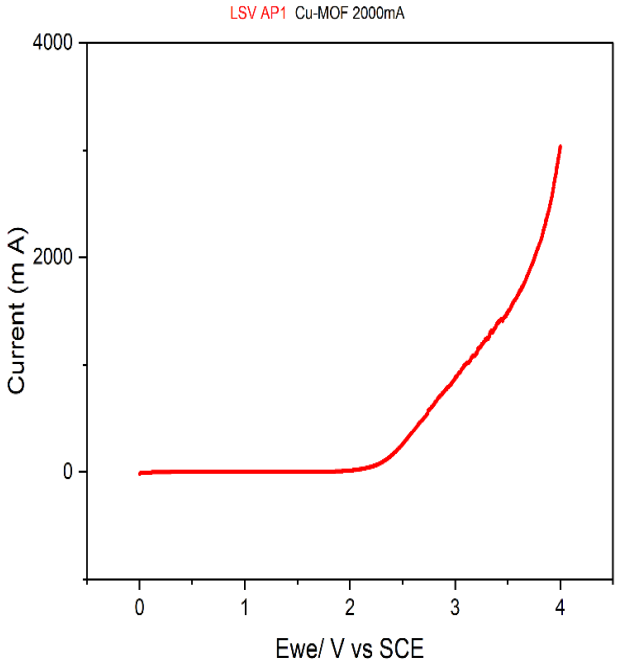

.

(e)

Figure 4.3.1C. Linear sweep voltammetry profiles of electrodes at identical applied potential conditions.

4.3.2 **AP3** Cu-MOF/Vulcan carbon **(**RAMP 20′ HT 30′)

Three electrodes were prepared with same catalyst material for different current densities. A current density dependent product trend was observed with CO selectivity peaking at 33.5% at 100 mA cm^{-2} while higher current density 300 mA cm^{-2} promoted C_2H_4 formation up to 31% (Figure 4.3.2A).Linear sweep voltammetry curves showed (Figure 4.3.2C) a significant increase in current density almost twice compare to AP1 Cu-MOF (RAMP 20′ HT 30′). Electrode potential curves over time at different applied current densities are demonstrated (Figure 4.3.2B).

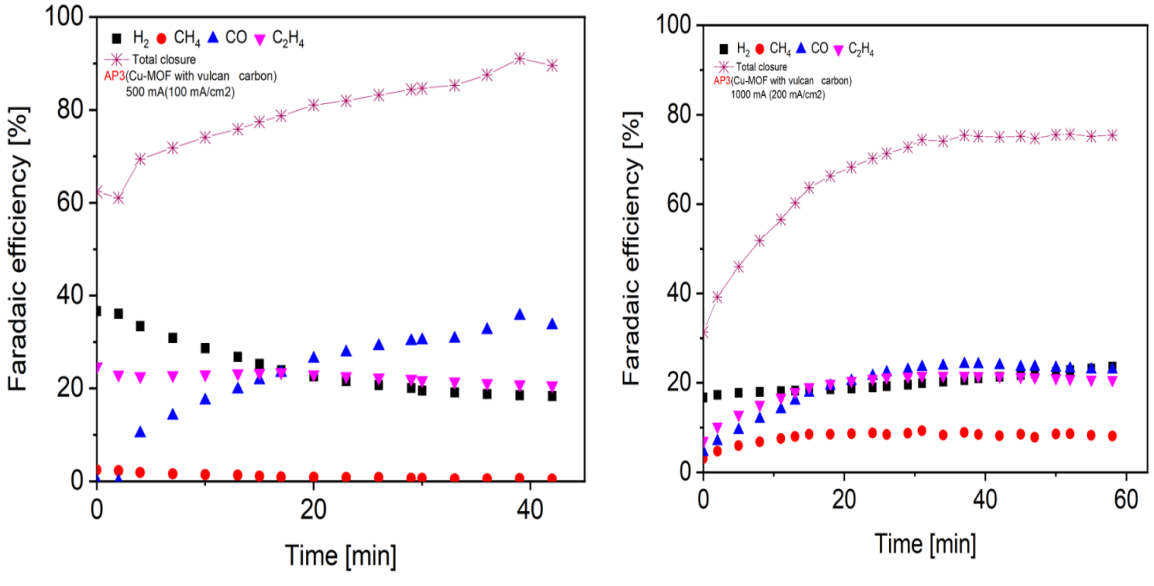

(a) **(b)**

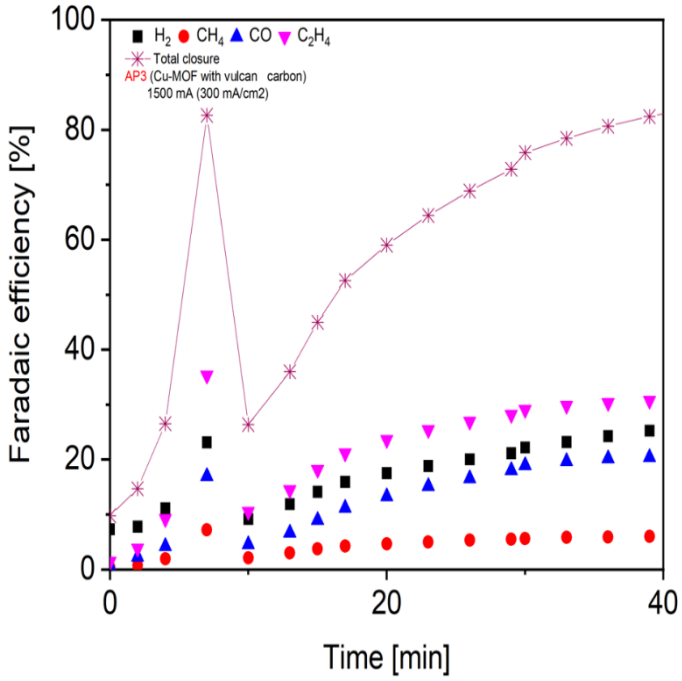

(c)

Figure 4.3.2. Evolution of faradaic efficiencies of gaseous products at constant applied current densities (a) 100 mA/cm^2(b) 200 mA/cm^2(c) 300 mA/cm^2

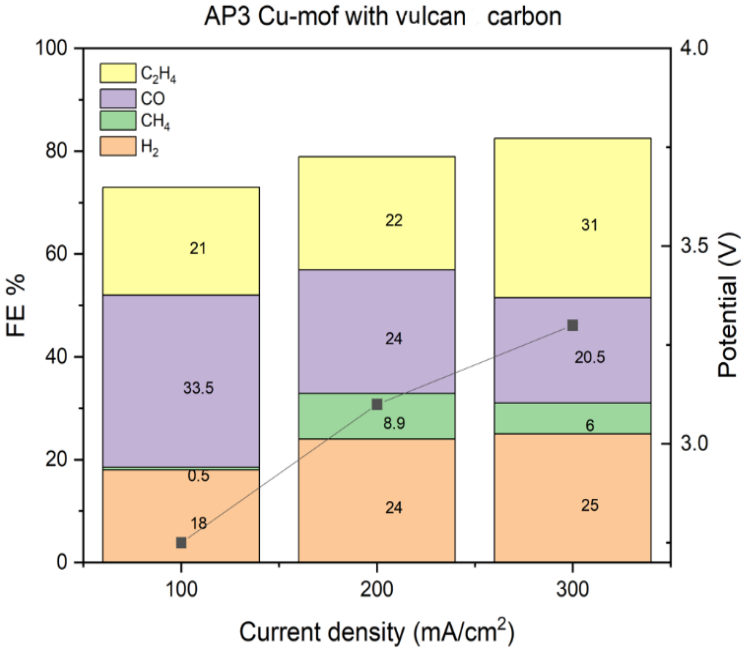

Figure 4.3.2A. Comparison of faradaic efficiencies of gaseous products at constant applied current densities.

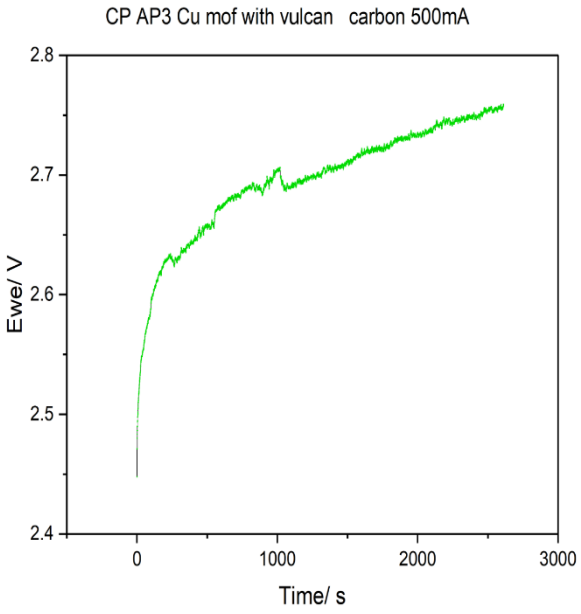

(a)

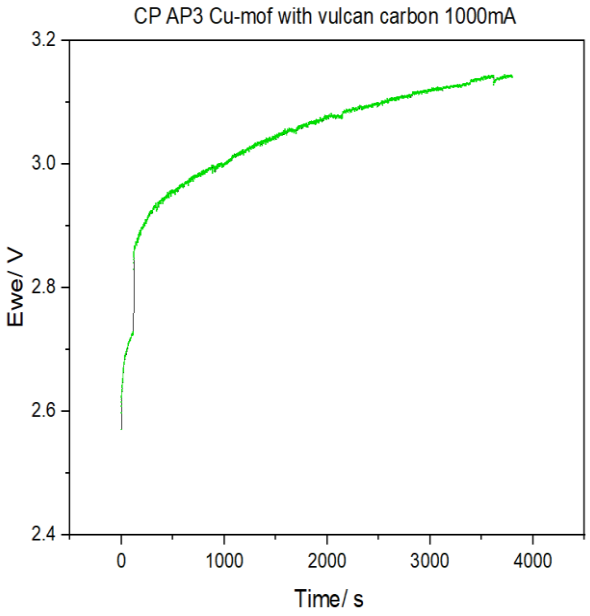

(b)

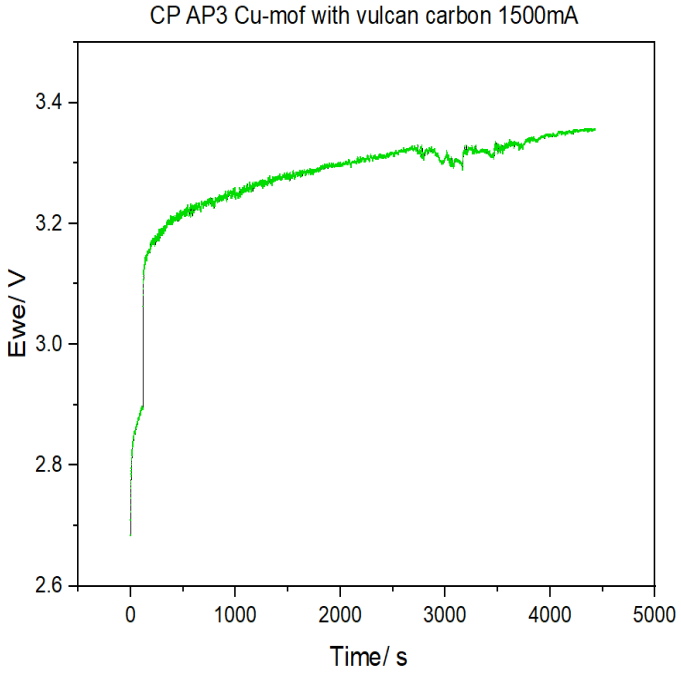

(c)

Figure 4.3.2B. Electrode potential curves over time at constant applied current densities (a) 100 mA/cm^2 (b) 200 mA/cm^2 (c) 300 mA/cm^2

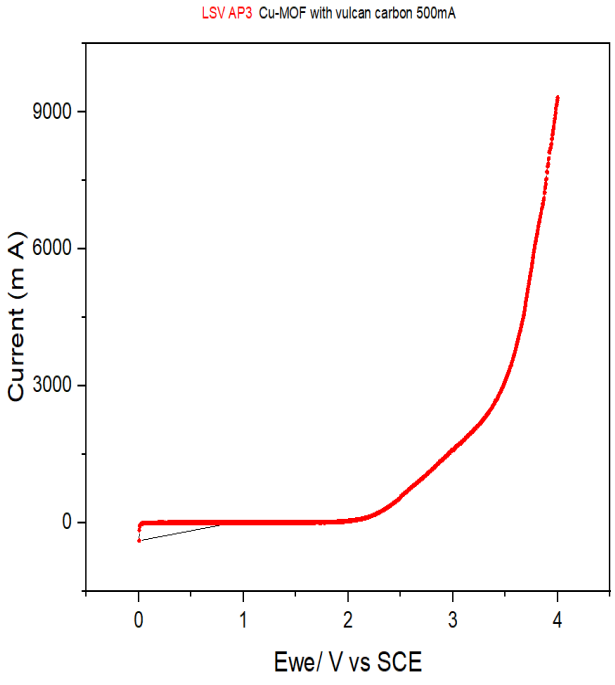

(a)

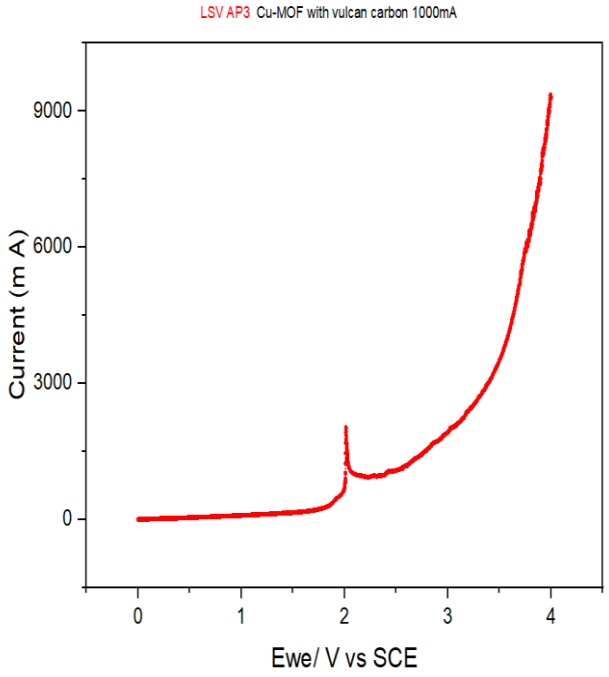

(b)

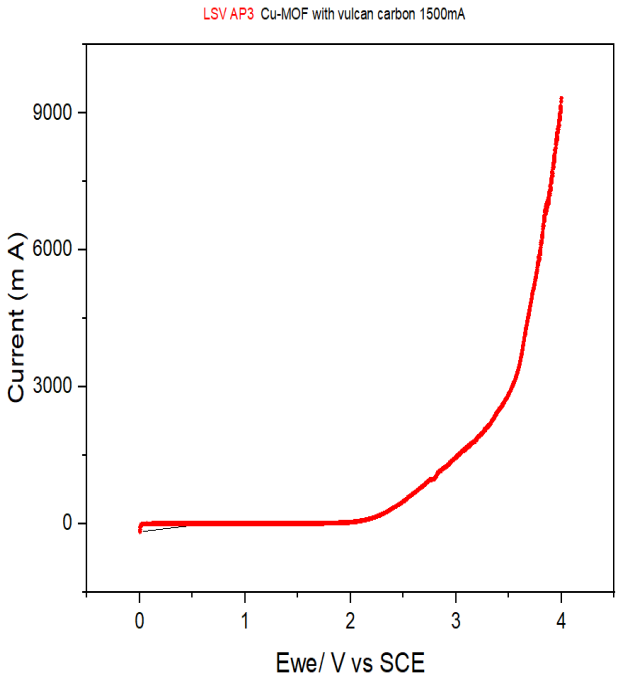

(c)

Figure 4.3.2C. Linear sweep voltammetry profiles of the electrodes at identical applied potential conditions.

4.3.3 **AP4** Cu-MOF/Vulcan carbon **(**RAMP 5′ HT 30′)

With same material two independent electrodes were prepared. At 200 mA cm^{-2} current density revealed that AP4 Cu-MOF/Vulcan carbon produced 23.5% CO while at 300 mA cm^{-2} produced 7 %. While no significant variation in C_2H_4 production was observed at two different applied current densities (Figure 4.3.3A). Linear sweep voltammetry curves showed (Figure 4.3.3C) a significant increase in current density almost twice compared to AP5 Cu-MOF (RAMP 5′ HT 30′). Electrode potential curves over time at different applied current densities are demonstrated (Figure 4.3.3B).

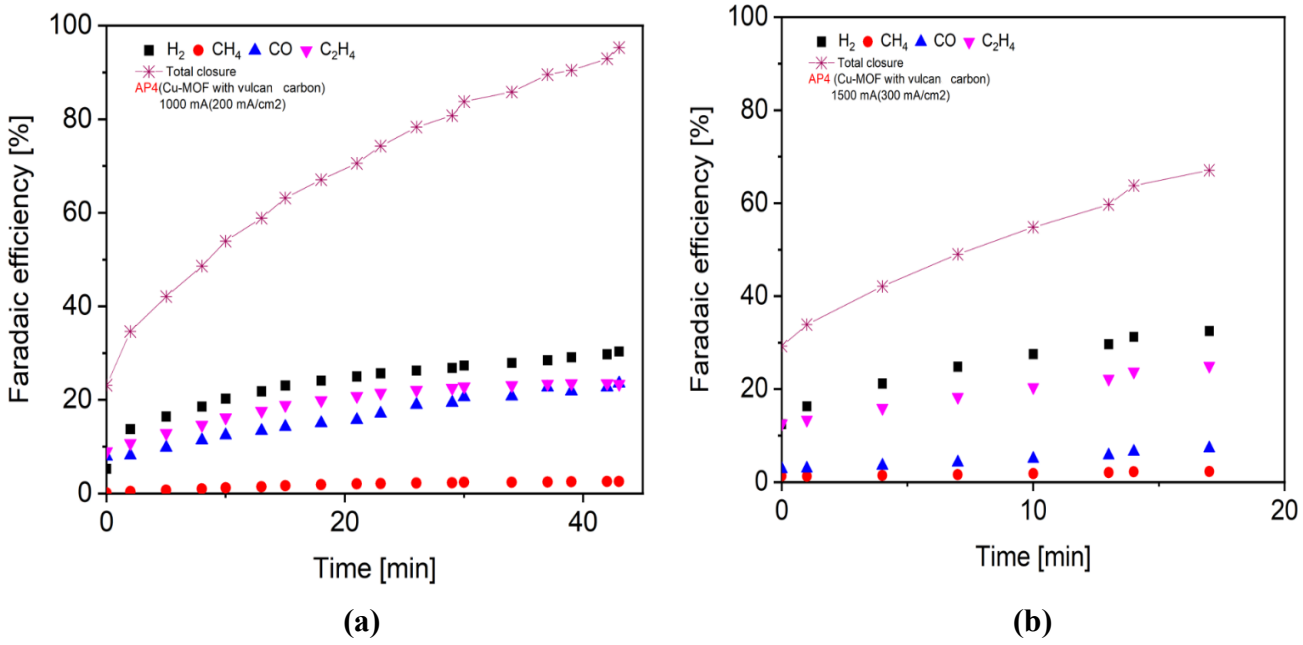

Figure 4.3.3. Evolution of faradaic efficiencies of gaseous products at constant applied current density (a) 200 mA/cm^2 (b) and 300 mA/cm^2

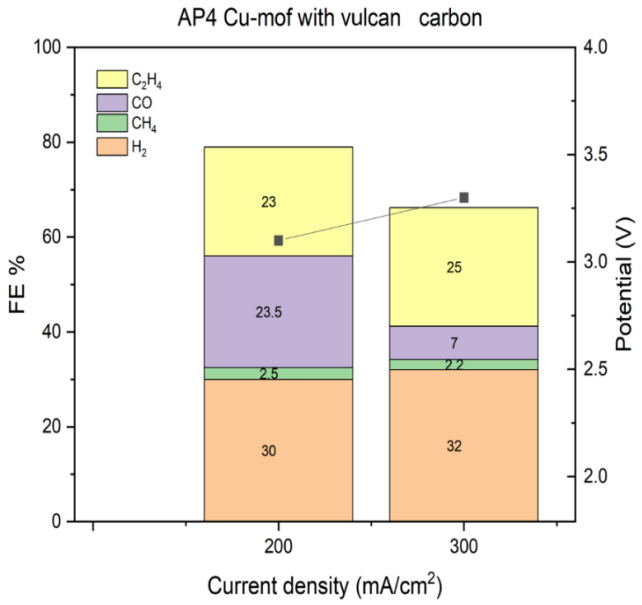

Figure 4.3.3A. Comparison of faradaic efficiencies of gaseous products at constant applied current densities.

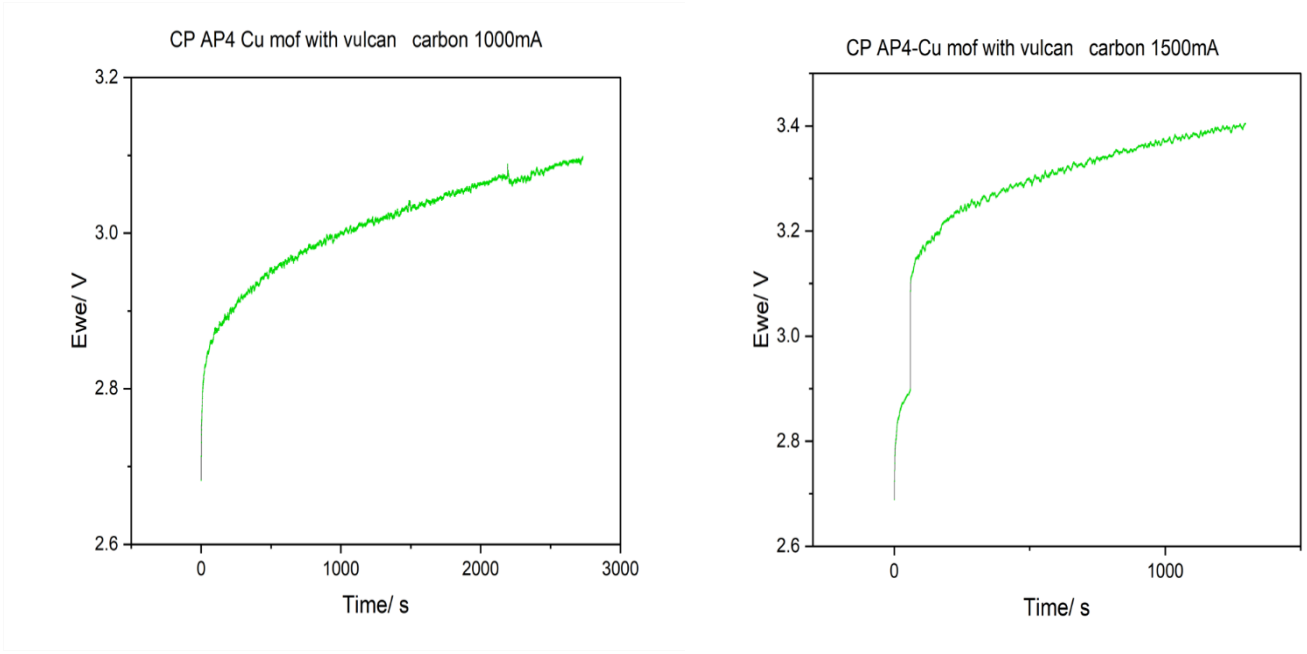

(a) **(b)**

Figure 4.3.3B. Electrode potential curves over time at constant applied current densities (a) 200 mA/cm^2 (b) 300 mA/cm^2

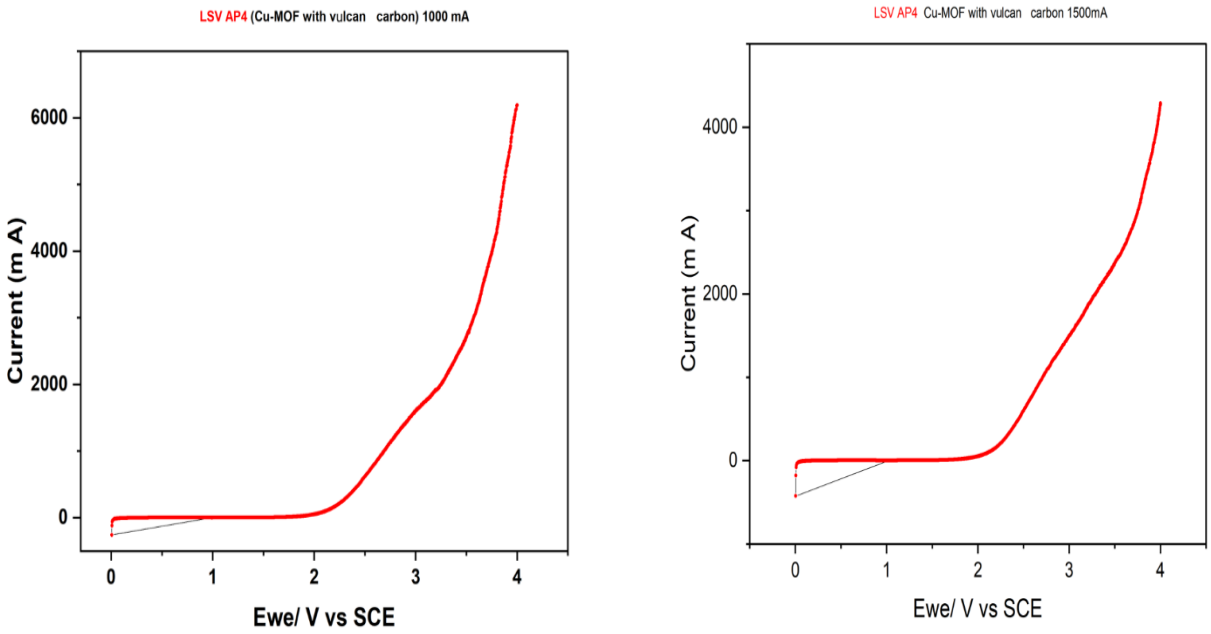

(a) **(b)**

Figure 4.3.3C. Linear sweep voltammetry profiles of electrodes at identical applied potential conditions.

4.3.4 **AP5** Cu-MOF **(**RAMP 5′ HT 30′)

Two electrodes were prepared with same material for two different current densities. With maximum selectivity of C_2H_4 up to 35% and CO 18% at 200 mA cm^{-2}. While at 300 mA cm^{-2} the production of CO reduced to 5% (Figure 4.3.4A). Linear sweep voltammetry curves showed (Figure 4.4.3C) almost half current density compared to AP4 Cu-MOF/Vulcan carbon (RAMP 5′ HT 30′).

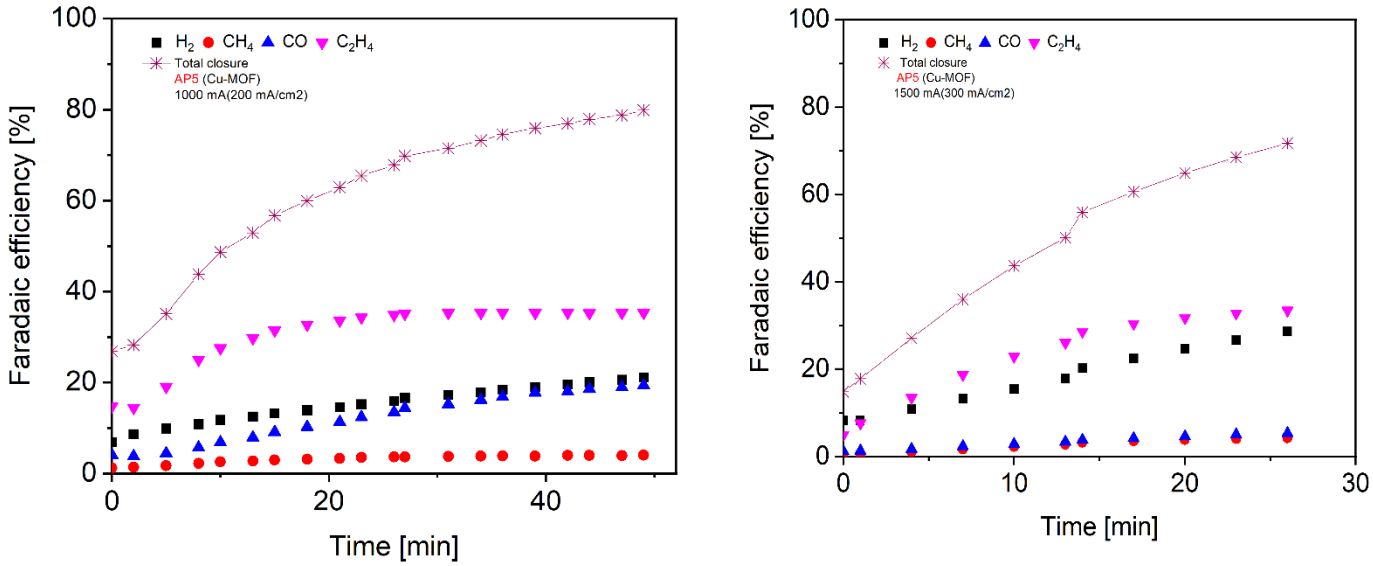

Figure 4.3.4. Evolution of faradaic efficiencies of gaseous products at constant applied current density (a) 200 mA/cm^2 (b) and 300 mA/cm^2

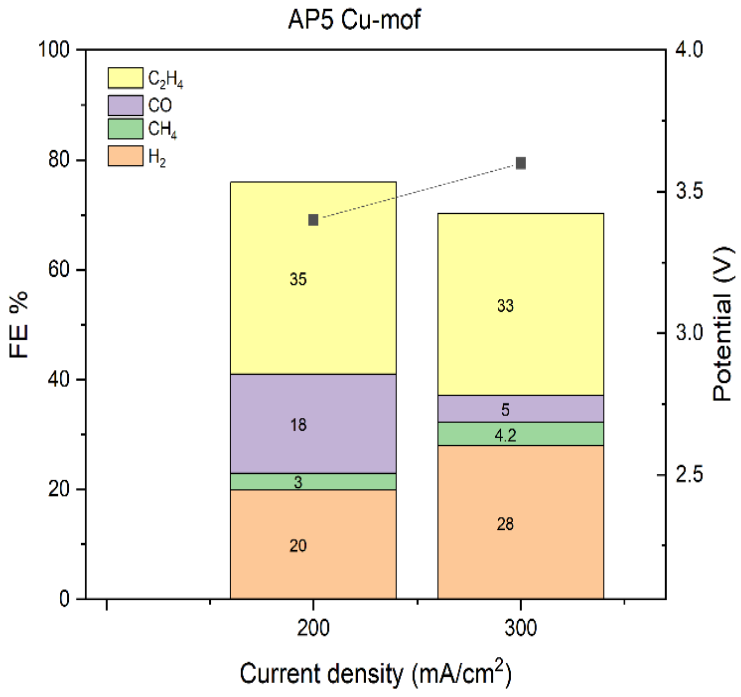

Figure 4.3.4A. Comparison of faradaic efficiencies of gaseous products at constant applied current densities.

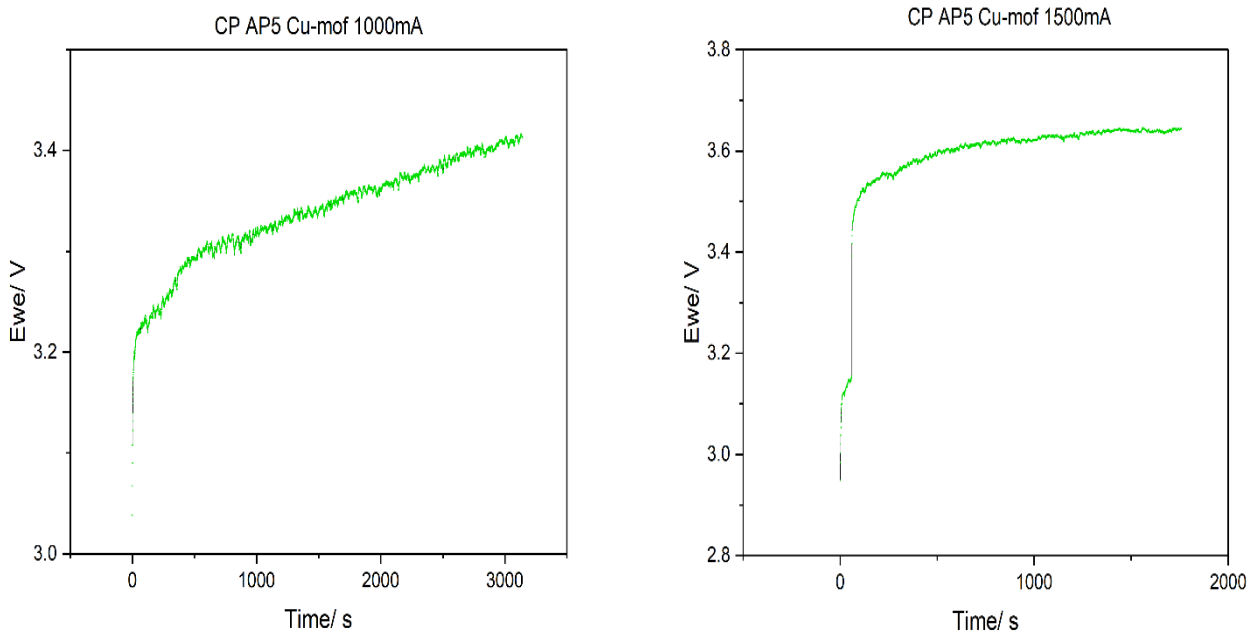

(a) **(b)**

Figure 4.3.4B. Electrode potential curves over time at constant applied current densities (a) 200 mA/cm^2 (b) and 300 mA/cm^2

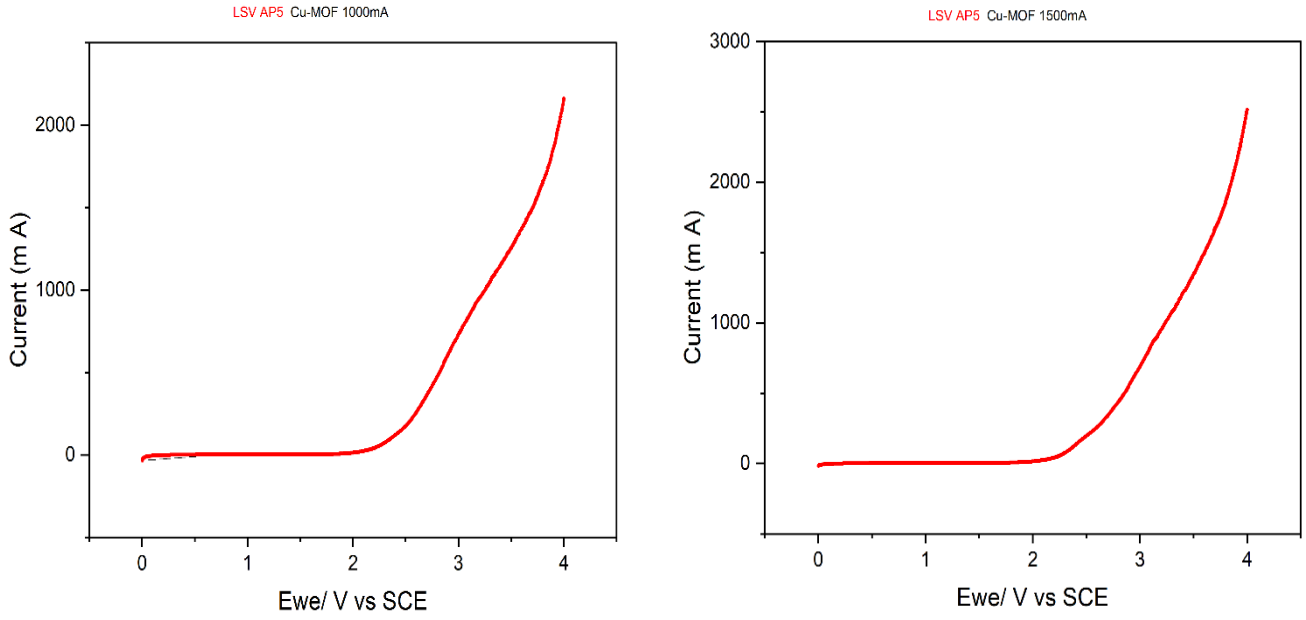

(a) **(b)**

Figure 4.3.4C. Linear sweep voltammetry profiles of electrodes at identical applied potential conditions.

4.3.5 **AP9** Cu-MOF Mesoporous carbon **(**RAMP 5′ HT 30′)

The synthesized catalyst exhibited higher selectivity toward C_2H_4 reaching up to 30%, CO 16% and CH_4 9.5% at current density 200 mA cm^{-2}, whereas at a higher current density of 300 mA cm^{-2} it produced 12.6 % CH_4 and C_2H_4 23% (Figure 4.3.5A).

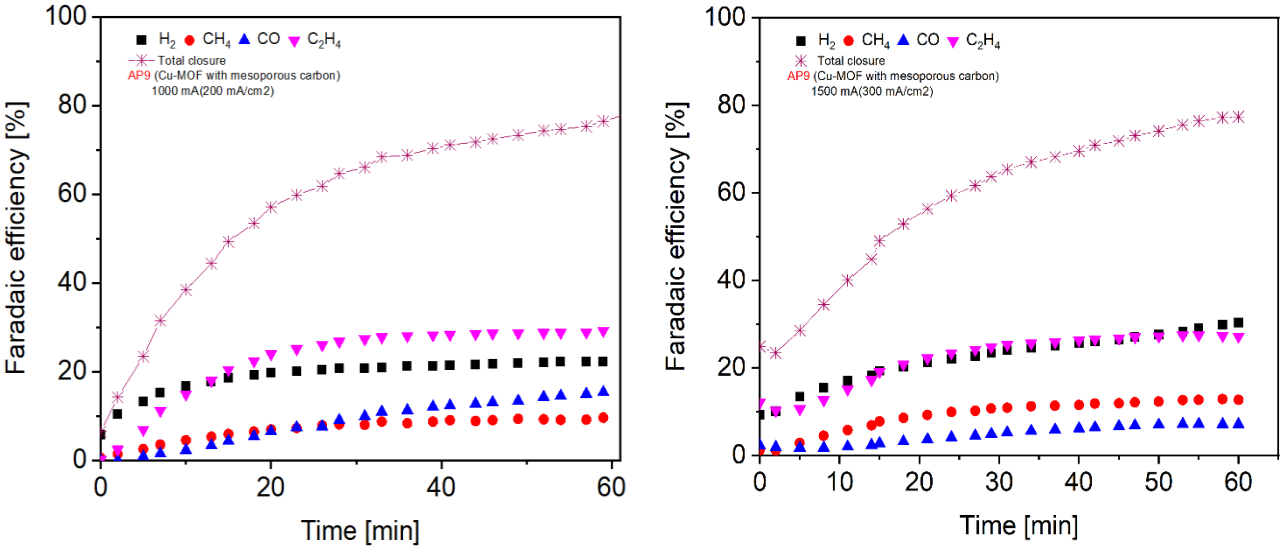

Figure 4.3.5. Evolution of faradaic efficiencies of gaseous products at constant applied current density (a) 200 mA/cm^2 (b) 300 mA/cm^2

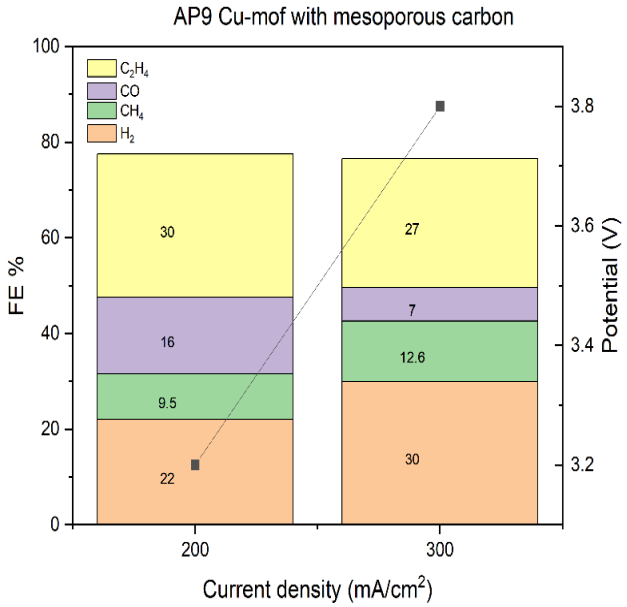

Figure 4.3.5A. Comparison of faradaic efficiencies of gaseous products at constant applied current densities.

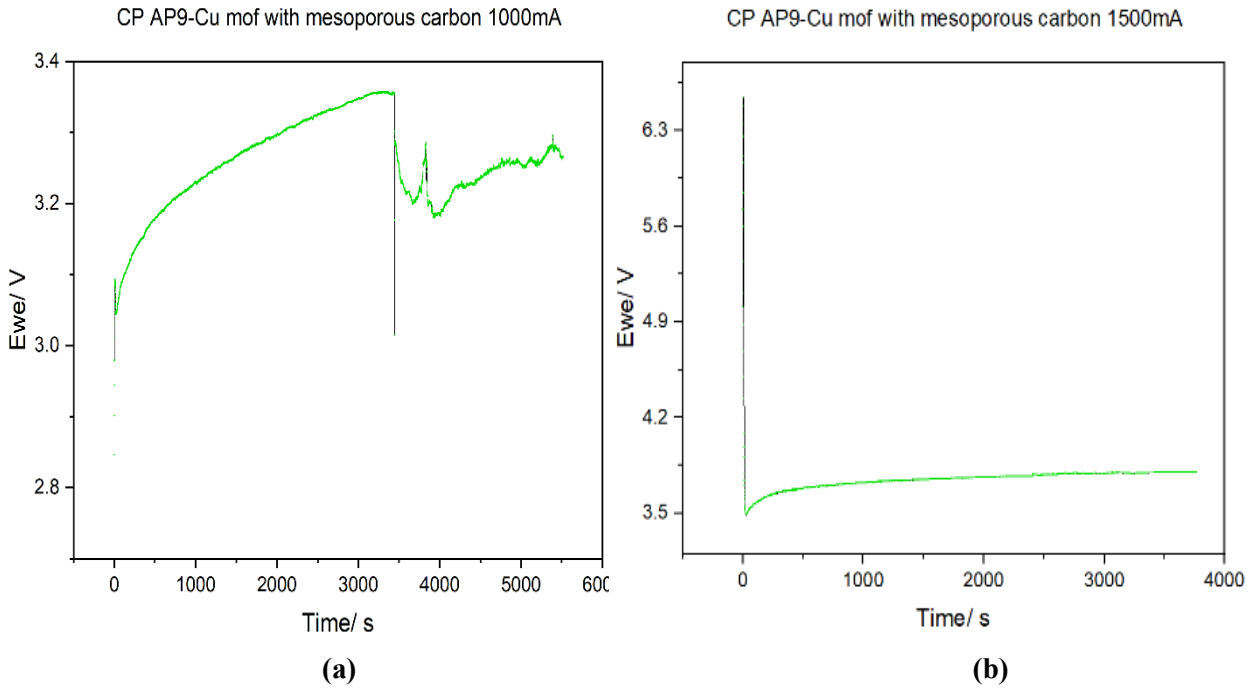

Figure 4.3.5B. Electrode potential curves over time at constant applied current densities (a) 200 mA/cm^2 (b) and 300 mA/cm^2

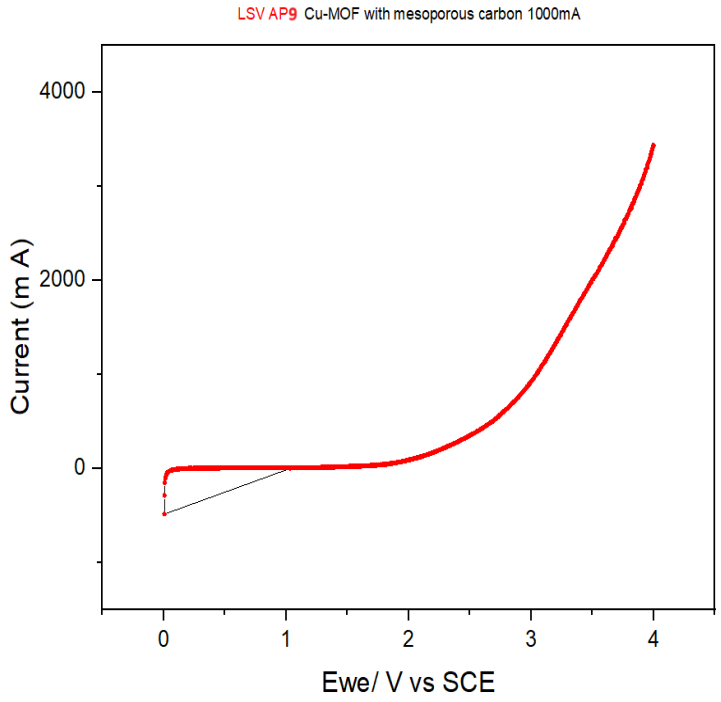

Figure 4.3.5C. Linear sweep voltammetry profile at specific applied potential.

4.4 Comparative analysis

4.4.1 RAMP effect in Cu-MOF

During microwave-assisted synthesis, AP1 Cu-MOF was prepared using a ramp of 20 minutes, whereas Cu-MOF AP5 was synthesized with a shorter ramp time of 5 minutes, while maintaining the same hold time 30 minutes. It was observed that the shorter ramp resulted in enhanced production of CO and CH_4 (Figure 4.4.1).

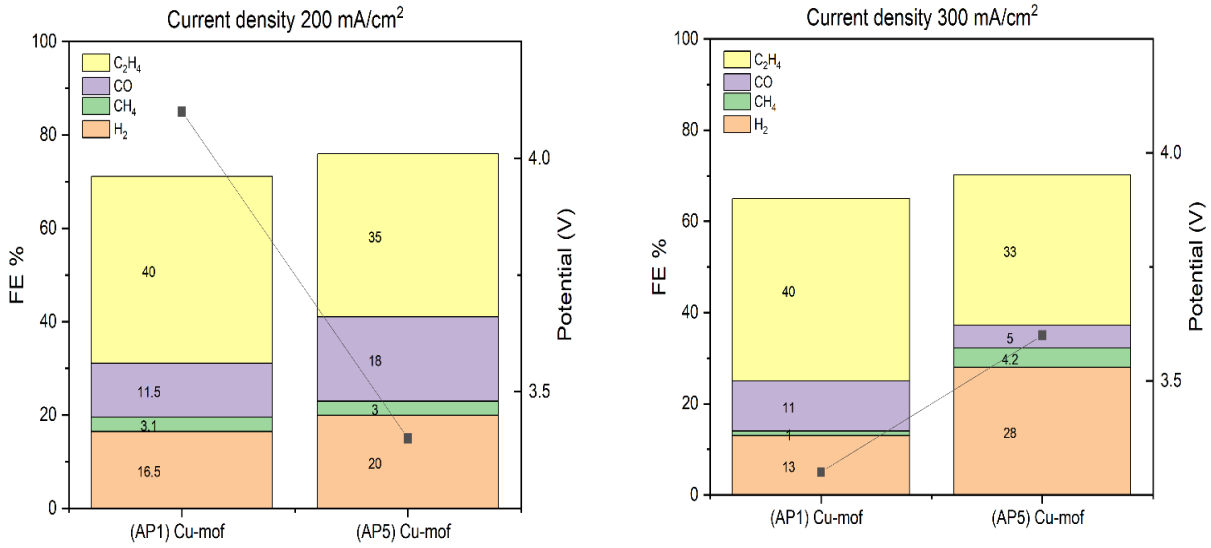

Figure 4.4.1. Faradaic efficiency of Cu-MOF catalyst under fixed hold time with different RAMP at different current densities.

4.4.2 RAMP effect in Cu-MOF/Vulcan carbon

At same hold time 30 minutes increasing the microwave ramp time from 5 to 20 minutes for AP3 Cu-MOF/Vulcan carbon synthesis led to improved methane and carbon monoxide formation at lower current density 200 mA cm^{-2} (Figure 4.4.2).

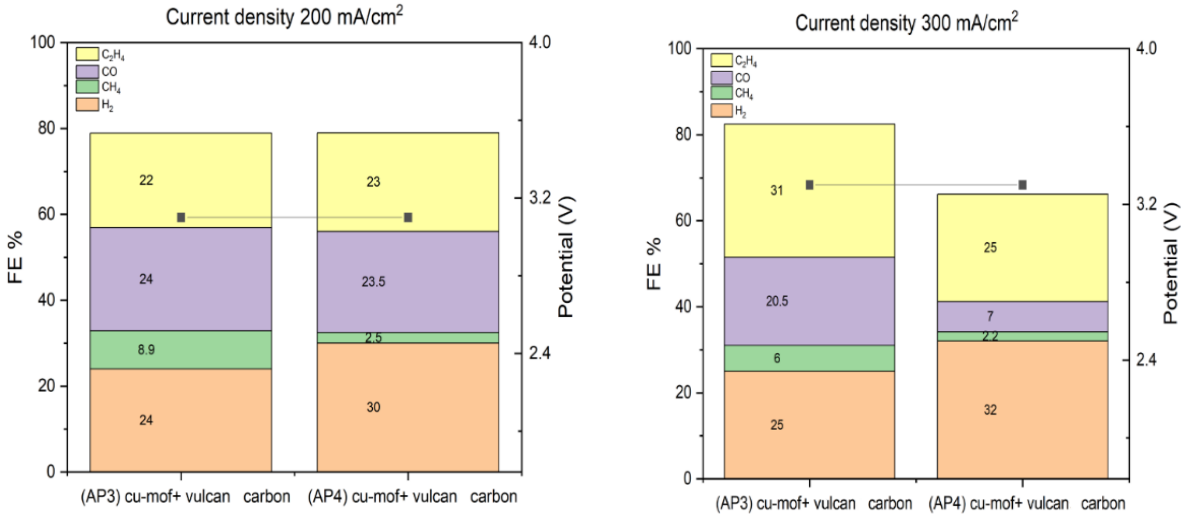

Figure 4.4.2. Faradaic efficiency of Cu-MOF/Vulcan Carbon under fixed hold time with different RAMP at different current densities.

4.4.3 Vulcan carbon effect in Cu-MOF

When synthesized under identical microwave conditions 5-minute ramp and 30-minute hold time the AP4 Cu-MOF/Vulcan carbon generated 23.5% CO at 200 mA cm^{-2} whereas AP5 Cu-MOF favored C_2H_4 formation with a Faradaic efficiency of 35% at same current density (Figure 4.4.3).

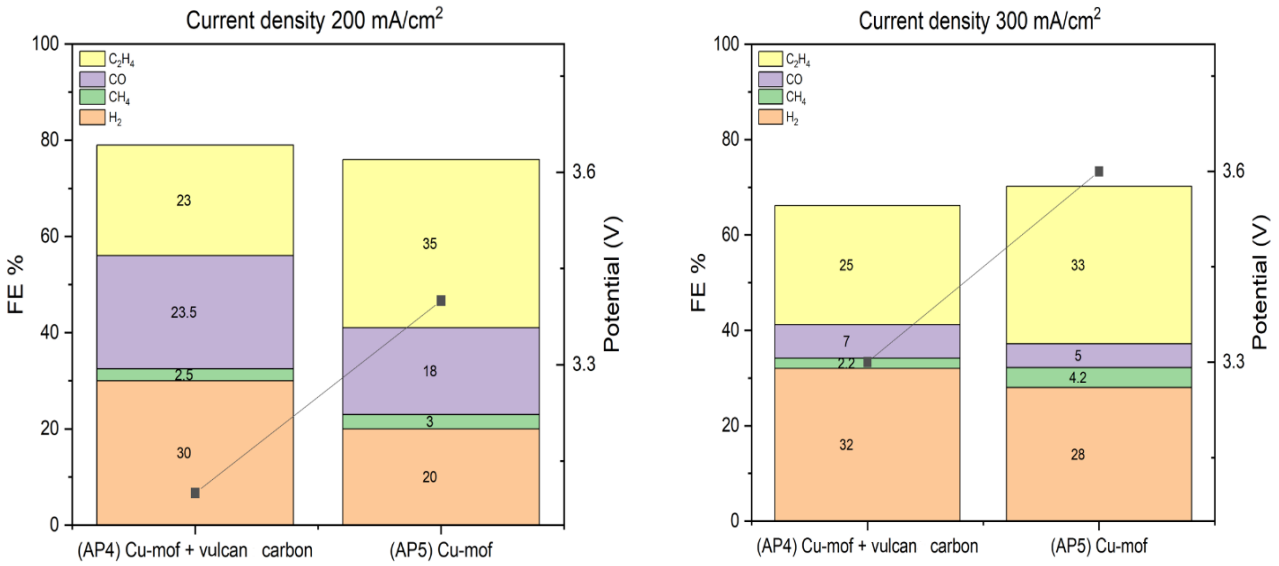

Figure 4.4.3. Faradaic efficiency of Cu-MOF and Cu-MOF/Vulcan Carbon under fixed RAMP and hold time at different current densities.

4.4.4 Mesoporous carbon effect in Cu-MOF

At constant synthesis parameters 5-minute ramp and 30-minute hold time AP9 Cu-MOF/Mesoporous carbon demonstrated improved methane generation over a wide current density range (Figure 4.4.4).

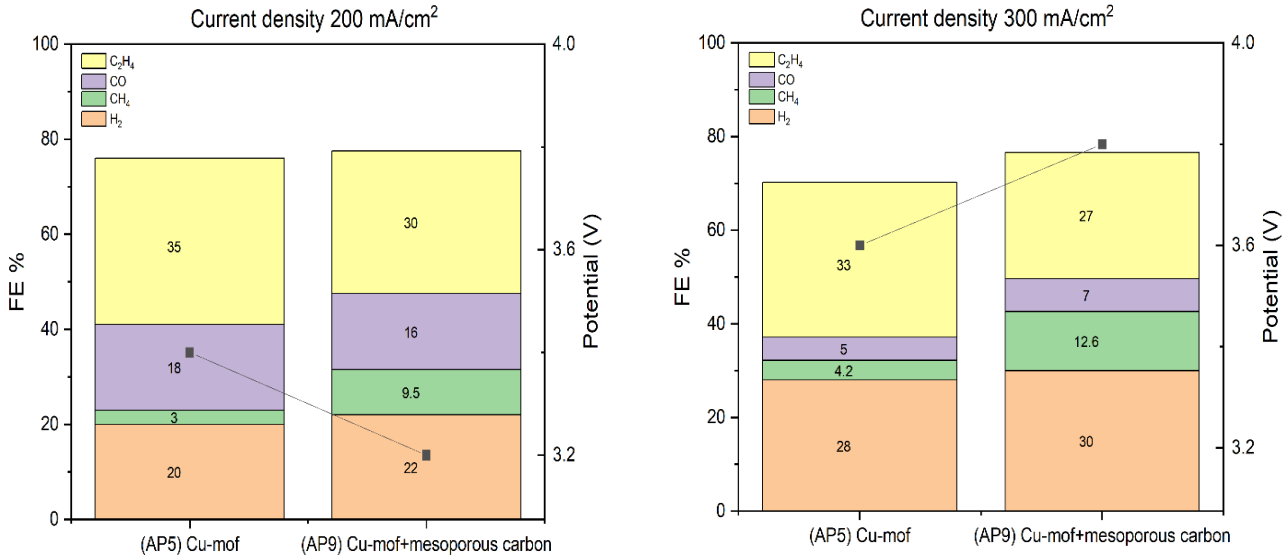

Figure 4.4.4. Faradaic efficiency of Cu-MOF and Cu-MOF/Mesoporous Carbon under fixed RAMP and hold time at different current densities.

4.4.5 Vulcan vs Mesoporous Carbon Effect in Cu-MOF

When synthesized with a 5 min ramp and 30 min hold time, AP9 Cu-MOF/Mesoporous carbon enhanced CH_4 production at both low and high current densities, while AP4 Cu-MOF/Vulcan carbon predominantly produced CO at lower current density (Figure 4.4.5).

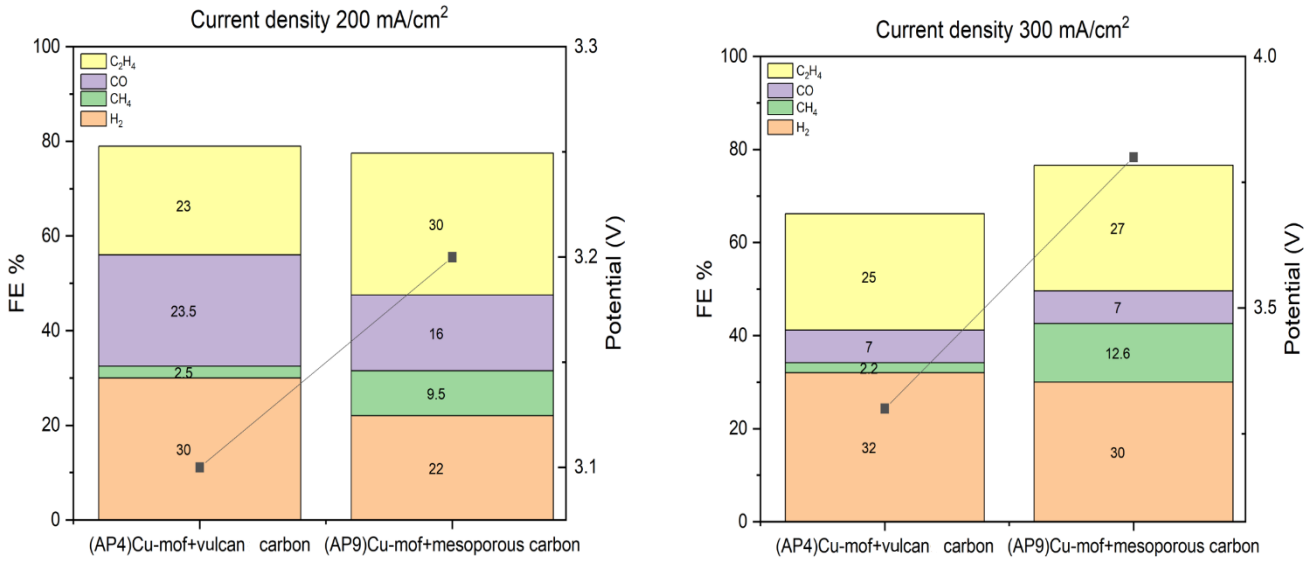

Figure 4.4.5. Faradaic efficiency of AP9 Cu-MOF/Mesoporous carbon and AP4 Cu-MOF/ Vulcan Carbon under fixed RAMP and hold time at different current densities.

5- CONCLUSION AND FUTURE DEVELOPMENTS

This study explored the synthesis structure performance relationship of Cu-MOF based electrocatalysts prepared via microwave assisted methods, with particular emphasis on the effect of ramp time, hold time, and carbon supports on electrochemical CO_2 reduction product distribution. The results demonstrate that microwave synthesis is a rapid and effective strategy for tailoring catalyst properties where subtle variations in heating profiles significantly influence catalytic selectivity.

Looking forward, further development of Cu-MOF based systems should focus on structural optimization, including defect engineering, morphology control, and linker functionalization to enhance active site accessibility. The exploration of advanced conductive supports such as graphene, carbon nanotubes, and heteroatom doping carbons may further improve electron transport and catalytic efficiency. In addition, incorporation of secondary metals or heteroatom dopants could modulate intermediate binding energies and promote higher value C2+ products.

Furthermore, in alignment with United Nation 2030 agenda [33] for sustainable development my research focuses on the electrochemical reduction converting carbon dioxide into valuable chemicals and fuels using sustainable energy. This work contributes primarily to sustainable development goals article 13 Climate Action for planet protection and article 7 sustainable affordable and Clean Energy by supporting carbon mitigation and the development of renewable based energy systems.

References

[1] NOAA Earth System Research Laboratory (2023). *Annual Greenhouse Gas Index (AGGI).* Available at: https://gml.noaa.gov/aggi/

[2] Chui, S. S.-Y., Lo, S. M.-F., Charmant, J. P. H., Orpen, A. G., & Williams, I. D. (1999). A chemically functionalizable nanoporous material $[Cu_3(TMA)_2(H_2O)_3]_n$. Science, 283(5405), 1148–1150. DOI: 10.1126/science.283.5405.1148.

[3] Jinli Qiao et al. "A review of catalysts for the electroreduction of carbon dioxide to produce low-carbon fuels". In: *Chem. Soc. Rev.* 43.2 (2014), pp. 631–675. DOI: 10.1039/c3cs60323g.

[4] Bijandra Kumar et al. "New trends in the development of heterogeneous catalysts for electrochemical CO 2 reduction". In: *Catalysis Today* 270 (July 2016), pp. 19–30. DOI: 10.1016/j.cattod.2016.02.006.

[5] Juqin Zeng et al. "Advanced Cu-Sn foam for selectively converting CO2 to CO in aqueous solution". In: *Applied Catalysis B: Environmental* 236 (Nov. 2018), pp. 475–482. DOI: 10.1016/j.apcatb.2018.05.056.

[6] Huan Xie et al. "Cu-based nanocatalysts for electrochemical reduction of CO2". In: *Nano Today* 21 (Aug. 2018), pp. 41–54. DOI: 10.1016/j.nantod.2018.05.001.

[7] James W. Vickers, Dominic Alfonso and Douglas R. Kauffman. "Electrochemical Carbon Dioxide Reduction at Nanostructured Gold, Copper, and Alloy Materials". In: *Energy Technology* 5.6 (Mar. 2017), pp. 775–795. DOI: 10.1002/ente.201600580.

[8] Simelys Hernández et al. "Syngas production from electrochemical reduction of CO2: current status and prospective implementation". In: *Green Chemistry* 19.10 (2017), pp. 2326– 2346. DOI: 10.1039/c7gc00398f.

[9] Sujat Sen, Dan Liu and G. Tayhas R. Palmore. "Electrochemical Reduction of CO2at Copper Nanofoams". In: *ACS Catalysis* 4.9 (Aug. 2014), pp. 3091–3095. DOI: 10.1021/cs500522g.

[10] Ki Dong Yang et al. "Morphology-Directed Selective Production of Ethylene or Ethane from CO2on a Cu Mesopore Electrode". In: *Angewandte Chemie International Edition* 56.3 (Dec. 2016), pp. 796–800. DOI: 10.1002/anie.201610432.

[11] Park, K. S., Ni, Z., Côté, A. P., Choi, J. Y., Huang, R., Uribe-Romo, F. J., Chae, H. K., O'Keeffe, M., & Yaghi, O. M. (2006). Exceptional chemical and thermal stability of zeolitic imidazolate frameworks. Proceedings of the National Academy of Sciences (PNAS), DOI: 10.1073/pnas.0602439103

[12] Yoshio Hori et al. "Selective Formation of C2 Compounds from Electrochemical Reduction of CO2at a Series of Copper Single Crystal Electrodes". In: *The Journal of Physical Chemistry B* 106.1 (Jan. 2002), pp. 15–17. DOI: 10.1021/jp013478d.

[13] Singh, M. K.; Krishnan, S.; Singh, K.; Rai, D. K. CNT Interwoven Cu-MOF: A Synergistic Electrochemical Approach for Solid-State Supercapacitor and Hydrogen Evolution Reaction. Energy & Fuels, 2024. DOI: 10.1021/acs.energyfuels.4c00811

[14] Shen, Y.-J.; Hsu, Y.-H.; Chang, Y.-C.; Ma, J.-J.; Peng, K.-S.; Lu, Y.-R.; Hsu, S.-H.; Hung, S.-F. Microenvironment Matters: Copper–Carbon Composites Enable a Highly Efficient Carbon Dioxide Reduction Reaction to C_2 Products. ACS Applied Materials & Interfaces, 2025. DOI: 10.1021/acsami.4c20586

[15] Anthony Vasileff et al. "Surface and Interface Engineering in Copper-Based Bimetallic Materials for Selective CO2 Electroreduction". In: *Chem* 4.8 (Aug. 2018), pp. 1809–1831. DOI: 10.1016/j.chempr.2018.05.001.

[16] Ieuan Thomas-Hillman, Andrea Laybourn, Chris Doddsand, Samuel W. Kingman "Realising the environmental benefits of metal organic frame works: Recent advances in microwave synthesis" J. Mater. Chem. A, 2018, 6,11564 DOI: 10.1039/c8ta02919a

[17] Bunaciu, A. A., Udriştioiu, E. gabriela, & Aboul-Enein, H. Y. (2015). X-Ray Diffraction: Instrumentation and Applications. In *Critical Reviews in Analytical Chemistry* (Vol. 45, Issue 4). https://doi.org/10.1080/10408347.2014.949616

[18] Yang Leng. *Materials Characterization*. Wiley-VCH, 7th Aug. 2013. 392 pp.URL: https://www.ebook.de/de/product/21246083/yang_leng_materials_characterization.html.

[19] Xiaojie She, Shu Ping Lau "Challenges and Opportunities in Electrocatalytic CO2 Reduction to Chemicals and Fuels". Chem. Int. Ed. 2022, 61, e202211396 International Edition: DOI.org/10.1002/anie.202211396

[20] Chen, C. · Li, Y. · Yang, P "Proton sponge promotion of electrochemical CO_2 reduction to multi-carbon products" P205-220January 19, 2022 DOI:10.1016/j.joule.2021.12.002

[21] A. Sacco, "Electrochemical impedance spectroscopy: Fundamentals and application in dye-sensitized solar cells," Renewable and Sustainable Energy Reviews, vol. 79, pp. 814–829, 2017.

[22] Park Bishnu P. Regmi and Masoud Agah. "Micro Gas Chromatography: An Overview of Crit- ical Components and Their Integration". In: *Analytical Chemistry* 90.22 (Oct. 2018), pp. 13133–13150. DOI: 10.1021/acs.analchem.8b01461.

[23] Satoshi Horikoshi and Nick Serpone. *Microwaves in Nanoparticle Synthesis*. Wiley VCH Verlag GmbH, 24th Apr. 2013. ISBN: 3527331972. URL: https://www.ebook.de/de/product/19688382/microwaves_in_nanoparticle_synthesis.html.

[24] Yang Leng. *Materials Characterization*. Wiley-VCH, 7th Aug. 2013. 392 pp. URL: https://www.ebook.de/de/product/21246083/yang_leng_materials_characterization.html.

[25] Robert A. Meyers. *Encyclopedia of Analytical Chemistry*. Wiley-Blackwell, 18th Feb. 2011. 2188 pp. ISBN: 0470973331. URL: https://www.ebook.de/de/product/13728875/robert_a_meyers_encyclopedia_of_analytical_chemistry.html.

[26] CNT interwoven Cu-MOF https://doi.org/10.1021/acs.energyfuels.4c00811

[27] Larry R. Faulkner Allen J. Bard. *Electrochemical Methods*. John Wiley & Sons Inc, 4th Dec. 2000. 864 pp. ISBN: 0471043729. URL: https://www.ebook.de/de/product/3254912/allen_j_bard_larry_r_faulkner_electrochemical_methods.html.

[28] Bishnu P. Regmi and Masoud Agah. “Micro Gas Chromatography: An Overview of Critical Components and Their Integration”. In: *Analytical Chemistry* 90.22 (Oct. 2018), pp. 13133–13150. DOI: 10.1021/acs.analchem.8b01461.

[29] Hideshi Ooka, Marta C. Figueiredo and Marc T. M. Koper. “Competition between Hydrogen Evolution and Carbon Dioxide Reduction on Copper Electrodes in Mildly Acidic Media”. In: *Langmuir* 33.37 (May 2017), pp. 9307–9313. DOI: 10 . 1021 / acs . langmuir.7b00696.

[30] Jonathan Rosen et al. “Electrodeposited Zn Dendrites with Enhanced CO Selectivity for Electrocatalytic CO2 Reduction”. In: *ACS Catalysis* 5.8 (July 2015), pp. 4586–4591. DOI: 10.1021/acscatal.5b00922.

[31] Microenvironment Matters: Copper−Carbon Composites Enable a Highly Efficient Carbon Dioxide RR to C2 Products https://doi.org/10.1021/acsami.4c20586

[32] He, Qiu-Ling, et al. "Copper ion based metal–organic framework nanomaterials with roughness enhanced protein adhesion for high-efficiency hemoglobin separation." *New Journal of Chemistry* 47.15 (2023): 7245-7252.

[33] UN 2030 Agenda for Sustainable Development https://unric.org/it/agenda-2030/